nature communications

Article

https://doi.org/10.1038/s41467-025-60244-z

Blood-triggered self-sealing and tissue adhesive hemostatic nanofabric

Received: 13 June 2024

Accepted: 20 May 2025

Published online: 27 May 2025

Check for updates

Yan Fang[1,2], Linyu Wang[1,2], Xinwei Zheng[1], Peng Ni[1], Zhibo Xu[1], Ziying Wang[1], Yunxiang Weng[1], Qinhui Chen[1] ✉ & Haiqing Liu[1] ✉

Current hemostatic fabric often encounters the issue of blood seeping or leaking through the fabric and at the junctions between the fabric and tissue, leading to extra blood loss. Herein, we report a hemostatic nanofabric composed of anionic and cationic nanofibers. Upon contact with wound, the porous nanofabric can absorb the interfacial blood and self-seal to form a compact physical barrier through interfiber bonding, preventing blood from longitudinally penetrating the fabric. This process results in the encapsulation of blood components within the electrostatically crosslinked nanofiber network, creating a robust thrombus that reinforces the physical barrier. Moreover, this nanofabric exhibits strong tissue adhesiveness, inhibiting blood seeping out at the seam of the fabric and tissue. Its hemostatic performance in animal injuries surpasses that of standard cotton gauze and Combat Gauze™. In the pig femoral artery injury, the blood loss from the nanofabric is only ca. 8% of that from Combat Gauze™. The nanofabric exhibits excellent biodegradability, hemocompatibility, cytocompatibility, antibacterial activity, and wound healing promotion.

Uncontrolled bleeding from trauma and surgery is the leading cause of death worldwide each year[1]. In civil emergencies, the majority of fatalities occur within 1 h following blunt trauma, while penetrating injuries can result in massive bleeding within 5 to 10 min[2]. Timely and efficient management of life-threatening bleeding can provide crucial time for further treatment and greatly decrease mortality rates. Currently, sutures, staples, and clips are the most commonly used methods in clinical settings to close wounds for hemostasis. However, these techniques are impractical outside of the surgical units and are rarely used in emergency situations[3]. To overcome this challenge, non-professional and easy-to-use hemostatic agents are imperative for bleeding control in pre-hospital occasions.

To date, various hemostatic materials in the forms of fabric, sponge, glue, hydrogel, and powder have been developed[4–10]. Hemostatic fabric remains the foremost choice for all forms of hemostasis due to its cost-effectiveness, scalability, wide applicability, and ease of storage, transport, and use[11]. The traditional hemostatic fabric is a sterile cotton gauze. The high hydrophilicity and porous nature of gauze allow for blood absorption and concentration of blood components. However, due to the limited clotting capability of this medical gauze, mechanical compression is necessary to facilitate stopping bleeding. Using this method to control bleeding in delicate and hemorrhage-prone organs, such as the heart, liver, and spleen, often leads to secondary damage[5]. Procoagulants such as kaolin, $CaCO_3$, and zeolite have been incorporated into hemostatic fabric to improve blood clotting[12–14]. These nanoclays can expedite blood coagulation reactions, resulting in rapid thrombus formation[15]. Despite this, blood can still penetrate through the pores of the hemostatic fabric and continue to seep, particularly in cases of hypertension. In order to address this issue, various strategies have been explored to modify the wettability of hemostatic fabric by applying a hydrophobic region[5,16–18]. For instance, Xu et al. used a hydrophobic paraffin-based coating on the back of a hydrophilic gauze[16]. Yap et al. developed a composite fabric by incorporating hydrophobic poly(vinylidene fluoride) onto carbon nanofibers[17]. Furthermore, our group introduced a flexible long hydrophobic alkyl chain terminated with a catechol group onto the

[1]College of Chemistry and Materials Science, Fujian Key Laboratory of Polymer Materials, Fujian Normal University, Fujian, China. [2]These authors contributed equally: Yan Fang, Linyu Wang. ✉e-mail: chenqh@fjnu.edu.cn; haiqingliu@fjnu.edu.cn

cotton gauze[5]. While this hydrophobic modification can impede the longitudinal penetration of blood through the hemostatic fabric, the issue of blood seepage at the seam between the fabric and tissue is frequently overlooked, leading to the wastage of valuable blood.

Herein, we aim to construct an advanced hemostatic nanofabric that can rapidly and effectively seal wounds in all directions to prevent blood outflow. The hemostatic nanofabric is composed of anionic and cationic nanofibers. These oppositely charged nanofibers within the hemostatic nanofiber fabric do not interact with each other after fabrication. However, upon contact with blood, the ionic nanofibers can bond together. This interfiber-bonding process facilitates the self-sealing of the hemostatic nanofabric, transforming its morphology from porous to a compact structure, effectively preventing longitudinal blood penetration. Furthermore, the hemostatic nanofiber fabric can firmly adhere to tissue, which can help prevent blood from seeping out at the seam between the fabric and tissue. In vivo hemostasis experiments have shown that the hemostatic nanofabric exhibits rapid and effective wound sealing abilities across various injury models, such as rat femoral artery injury, rat liver laceration, pig femoral artery injury, and pig liver laceration. The hemostatic properties of this fabric surpass those of commercial hemostatic fabrics including cotton gauze and Combat Gauze™. Moreover, the hemostatic nanofiber fabrics display excellent hemocompatibility, cytocompatibility, and biodegradability. This eliminates the necessity for removal from the body post-hemostasis, thereby minimizing the risk of secondary wound injury and re-bleeding. The hemostatic nanofiber fabric offers advantages such as instant water-triggered interfiber bonding, tissue adhesiveness, biocompatibility, biodegradability, antibacterial activity, low cost, and ease of use, making it a promising hemostatic dressing for diverse medical applications.

Results

Preparation, morphology, and breathability of QCS@PVA/CA@PVA nanofabric

The hemostatic nanofabric was prepared using the double-coaxial electrospinning technique. As shown in Fig. 1a, quaternized chitosan (QCS) serves as the sheath with polyvinyl alcohol (PVA) as the core, resulting in cationic QCS@PVA nanofibers. Additionally, catechol-modified sodium alginate (CA) acts as the sheath with PVA as the core, leading to the formation of anionic CA@PVA nanofibers. The cationic QCS@PVA nanofibers and anionic CA@PVA nanofibers were produced separately from two individual coaxial injectors but collected onto the same collection plate to create an anionic and cationic QCS@PVA/CA@PVA nanofabric. PVA is chosen for the core layer to offer structural support and stability to the fabric, utilizing its favorable mechanical property, biodegradability, and biocompatibility[19]. Both QCS and CA are polysaccharide derivatives known for their excellent biocompatibility, biodegradability, nontoxicity, low-cost, and wide availability[20]. Moreover, QCS contains positively charged quaternary amine groups, whereas CA contains negatively charged carboxyl groups and tissue adhesive catechol groups. The presence of these functional groups (e.g., quaternary amine, carboxyl, and catechol groups) in QCS and CA, will facilitate the interaction between QCS@PVA nanofibers and CA@PVA nanofibers upon contact with water, as well as promote the interaction between these ionic nanofibers and the tissue. In addition, other nanofiber fabrics were also prepared as controls, including PVA nanofabric composed of PVA nanofibers, QCS@PVA nanofabric composed of cationic QCS@PVA nanofibers, and CA@PVA nanofabric composed of anionic CA@PVA nanofibers.

Figure 1b shows the fluorescence microscopy image of the QCS@PVA/CA@PVA nanofabric, where QCS and CA were labeled by fluorescein isothiocyanate and Rhodamine B, respectively. The oppositely charged ionic fibers were observed to be randomly arranged without interfiber bonding. QCS@PVA/CA@PVA nanofabric displayed porous structures consisting of nanofibers with diameters ranging from 100 to 400 nm (Fig. 1c). Additionally, TEM analysis showed that both QCS@PVA nanofiber and CA@PVA nanofiber exhibited a core-shell structure, with a core diameter of approximately 300 nm and a shell thickness of around 10 nm, as illustrated in Fig. 1d, e. The tensile stress and strain of QCS@PVA/CA@PVA nanofabric was respectively up to 1.85 MPa and 162% (Supplementary Fig. 1). Furthermore, as show in Fig. 1f, g, we observed that the QCS@PVA/CA@PVA nanofabric can wrap around human fingers and can be tied into a bow. In addition, an ideal hemostatic fabric should have good air permeability, allowing air to freely penetrate the fabric. This enables the wound to receive sufficient oxygen supply to inhibit the propagation of anaerobes[11]. Thanks to its porous structure, the QCS@PVA/CA@PVA nanofabric exhibited good air permeability, with a water vapor transmission rate (WVTR) of 2186 g/m^{2}d, which was as good as that of cotton gauze (2592 g/m^{2}d) and Combat Gauze™ (2458 g/m^{2}d) (Fig. 1h, i).

Water blocking study I: Water-triggered interfiber bonding to form compact barrier for inhibiting water penetration

To evaluate the water-blocking capabilities of the QCS@PVA/CA@PVA nanofabric, an experiment was conducted using a glass tube with a height of 200 mm and a diameter of 23 mm. One end of the tube was covered with two layers of the QCS@PVA/CA@PVA nanofabric, each with a thickness of 0.2 µm. Red dyed deionized water was introduced at the other end. Under the condition of being free of any adhesive, QCS@PVA/CA@PVA nanofabric can adhere securely to the glass wall. Even under continuous water injection, the fabric remained securely in place without detachment. Furthermore, no water seeped through the QCS@PVA/CA@PVA nanofabric. Even after 90 min, the liquid-blocking performance of the QCS@PVA/CA@PVA nanofabric was maintained, as demonstrated by the stable liquid level observed under a water pressure of 19.6 kPa (Fig. 2a, Supplementary Movie 1). For the control groups, PVA nanofabric, QCS@PVA nanofabric, and CA@PVA nanofabric required a rubber band for securement. Meanwhile, water can penetrate through the PVA nanofabric, QCS@PVA nanofabric, and CA@PVA nanofabric (Fig. 2a). At around 1 min into the experiment, tiny water droplets were observed forming on the bottom surface of the PVA nanofiber fabric (Supplementary Fig. 2). As time progressed, these droplets merged together to form larger droplets, eventually succumbing to gravity and falling off the surface. By the 90 min, the liquid level in the tube decreased by ca. 60% (Fig. 2a). Similar poor liquid-blocking performance were observed on the QCS@PVA nanofabric and CA@PVA nanofabric (Fig. 2a and Supplementary Fig. 2). For the commercial hemostatic fabric including cotton gauze and Combat Gauze™, they also required a rubber band for securement. Upon introduction of water into the glass tube, water quickly permeated through the cotton gauze and Combat Gauze™ within 3 s (Supplementary Fig. 3). Blood penetrated these hemostatic fabrics in a manner similar to that of water. As demonstrated in Supplementary Fig. 4, blood was able to readily penetrate the PVA nanofabric, QCS@PVA nanofabric, and CA@PVA nanofabric, but was effectively blocked by the QCS@PVA/CA@PVA nanofabric. These results indicate that the QCS@PVA/CA@PVA nanofabric exhibits excellent inhibition of blood penetration. In general, the ability of liquid to flow through fabric under gravity is directly linked to the size of the fabric pores. The surface morphology of the fabrics before and after wetted by water was examined using SEM. Cotton gauze and Combat Gauze™ exhibited a variety of pores, including macropores with a diameter of approximately 500 µm located among yarns and micropores with a diameter of around 20 µm within fibers (Supplementary Fig. 5), which facilitated water penetration. In contrast, the PVA nanofabric, QCS@PVA nanofabric, and CA@PVA nanofabric showed significantly smaller micropores with a diameter of around 10 µm compared to cotton gauze and Combat Gauze™ (Fig. 2b).

https://doi.org/10.1038/s41467-025-60244-z

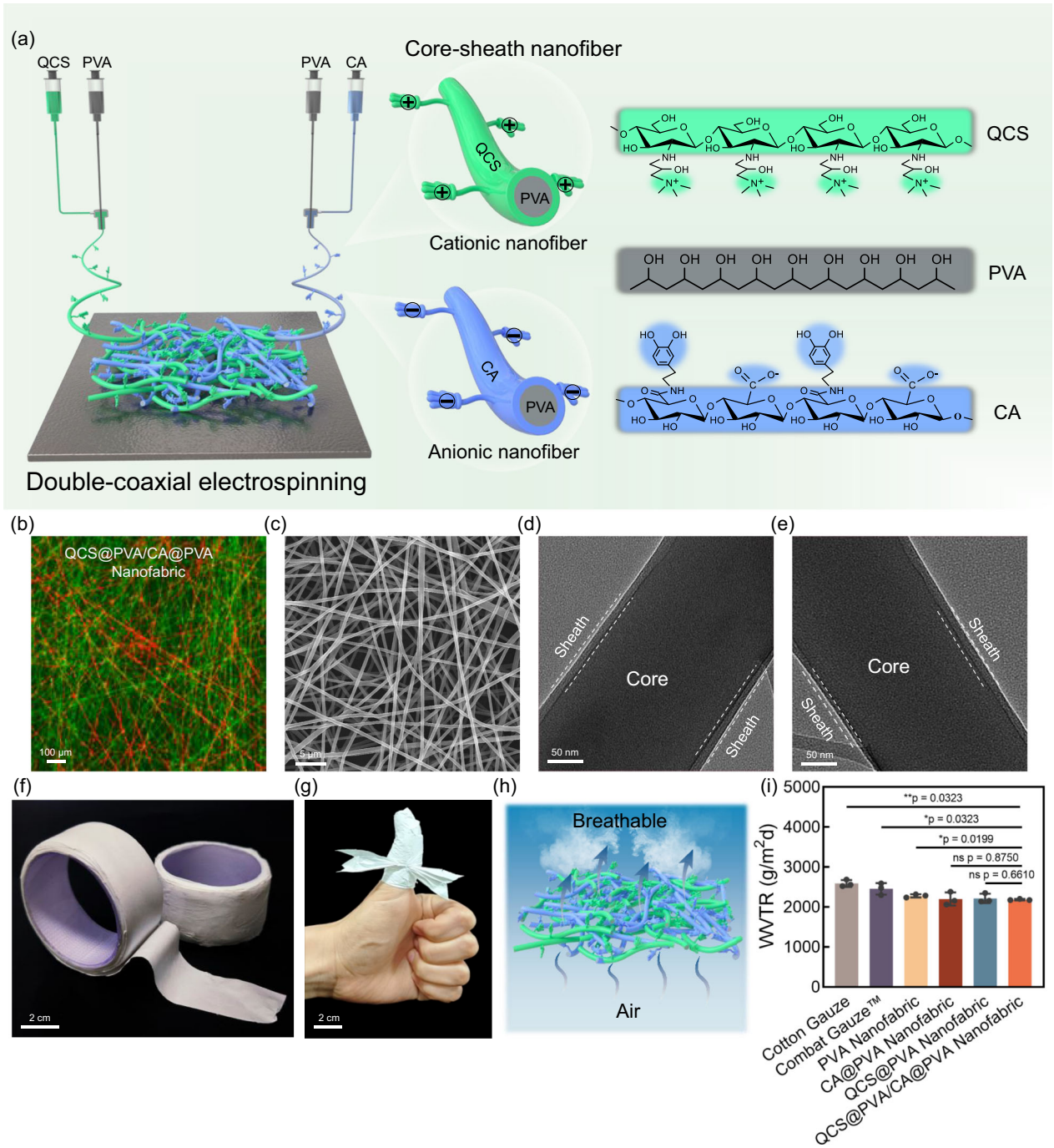

Fig. 1 | Fabrication of QCS@PVA/CA@PVA nanofabric via coaxial electrospinning and their multiscale structural and property characterization. **a** Schematic representation of the preparation of QCS@PVA/CA@PVA nanofabric using double-coaxial electrospinning technology. **b** A merged image by overlaying green (QCS) and red (CA) fluorescence microscope images of QCS@PVA/CA@PVA nanofabric. **c** SEM images of QCS@PVA/CA@PVA nanofabric. **d**, **e** TEM images of QCS@PVA nanofiber and CA@PVA nanofiber. **f**, **g** Photographs of QCS@PVA/CA@PVA nanofabric. **h** Schematic representation of the breathability of QCS@PVA/CA@PVA nanofabric. **i** WVTR of cotton gauze, Combat Gauze™, PVA nanofabric, QCS@PVA nanofabric, CA@PVA nanofabric, and QCS@PVA/CA@PVA nanofabric. (n = 3 independent samples; Student's t test; two-tailed; error bars = SD; data are presented as mean ± SD; ns = not significant; $^{*}p < 0.05$; $^{**}p < 0.01$). In **b**-**e**, the representative fluorescence microscope images, SEM images, and TEM images are shown (at least three images were taken for each sample). In **f**, **g** images from one representative experiment of three independent experiments are presented.

Consequently, the water penetration rate of PVA nanofabric, QCS@PVA nanofabric, and CA@PVA nanofabric was lower than that of cotton gauze and Combat Gauze™. After water wetting, the PVA nanofabric, QCS@PVA nanofabric, and CA@PVA nanofabric largely maintained their porous nanofibrous structure, with slightly increasing fiber diameter due to swelling and merging. However, the QCS@PVA/CA@PVA nanofabric transformed into a compact membrane without noticeable fibers and pores. This suggests that the nanofibers of QCS@PVA/CA@PVA nanofabric can electrostatically interact with each other in water to form a compact structure that prevents water penetration. Moreover, the interfiber bonding process was very fast, as shown in Supplementary Fig. 6, after being wetted with water for 3 s, the QCS@PVA/CA@PVA nanofabric had already formed a compact structure. Such rapid

https://doi.org/10.1038/s41467-025-60244-z

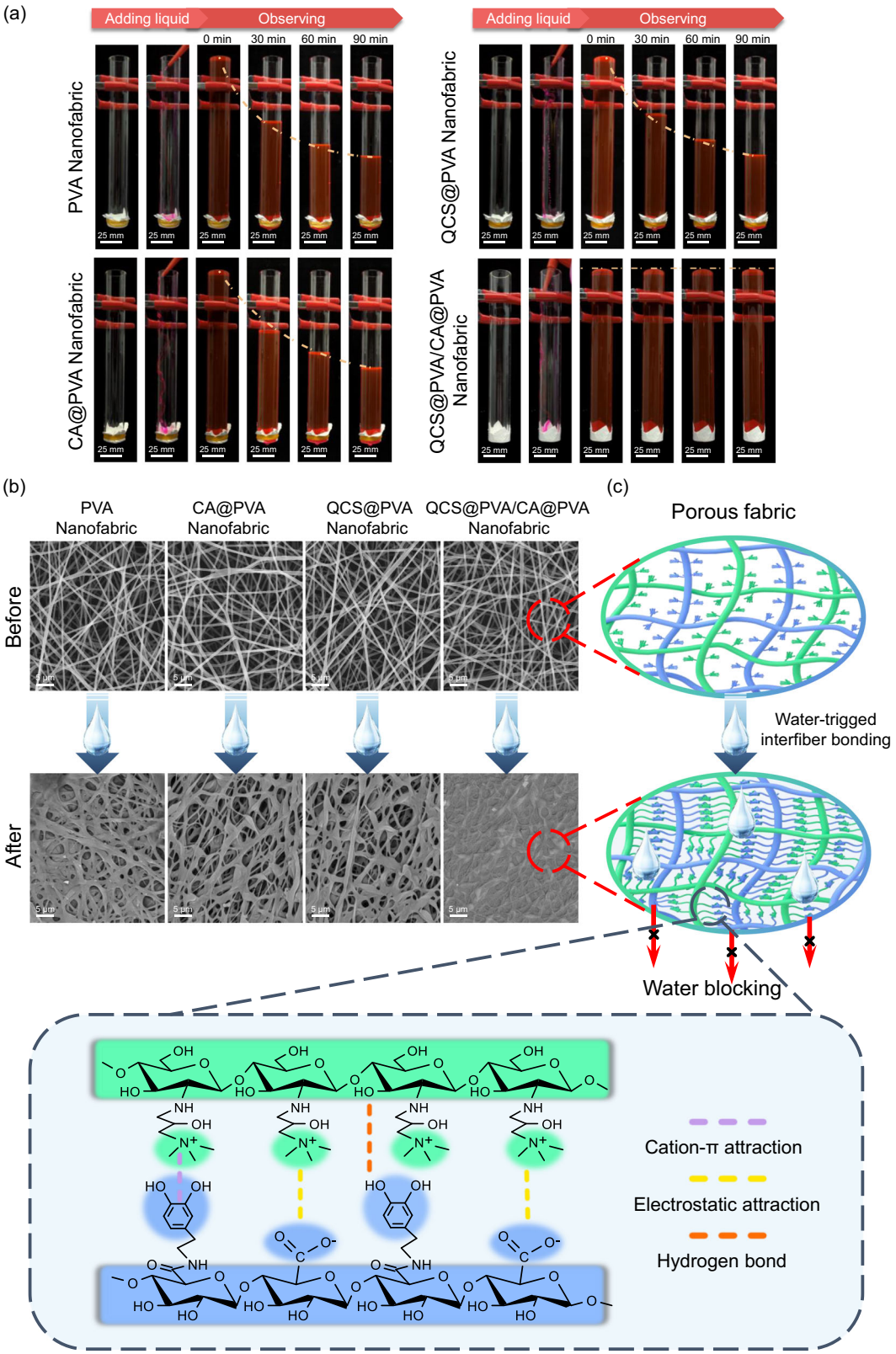

Fig. 2 | Water-triggered interfiber bonding to form compact barrier for inhibiting water penetration. a Water penetrated through PVA nanofabric, QCS@PVA nanofabric, and CA@PVA nanofabric, but was blocked by QCS@PVA/CA@PVA nanofabric. The water was dyed red by Rhodamine B. Yellow dashed lines mark the trajectory of liquid level descent. **b** SEM images of PVA nanofabric, QCS@PVA nanofabric, CA@PVA nanofabric, and QCS@PVA/CA@PVA nanofabric before and after wetted by water. **c** Scheme representation of the water blocking mechanism of QCS@PVA/CA@PVA nanofabric. In **a**, images from one representative experiment of three independent experiments are presented. In **b**, the representative SEM images are shown (at least three images were taken for each sample).

morphology transformation can meet the needs of emergency hemostasis. To investigate the structural evolution of QCS@PVA/CA@PVA nanofabric upon hydration, comprehensive spectroscopic analyses including XPS, FTIR, and Raman spectroscopy were systematically conducted. XPS analysis revealed a notable shift in binding energies following water treatment: the binding energy associated with the $-N^+(CH_3)_3$ groups of QCS decreased from 403.2 eV to 402.6 eV, while the binding energy corresponding to the C=O groups of CA increased from 533.3 eV to 534.7 eV (Supplementary Fig. 7a). These shifts in binding energy are attributed to the establishment of electrostatic interactions between the COO^- groups of CA and the $-N^+(CH_3)_3$ groups of QCS, which alter the electronic environments of the nitrogen and oxygen atoms[21,22]. Furthermore, the absorbance peak corresponding to the O–H and N-H stretching vibration broadened and exhibited a redshift from 3404 cm^{-1} to 3374 cm^{-1} upon wetting, indicating the formation of new hydrogen bonds between fibers[23]. The asymmetric stretching vibration of COO^- showed a blueshift from 1648 cm^{-1} to 1655 cm^{-1}, while the C–H bending vibration of $-N^+(CH_3)_3$ broadened and redshifted from 1482 cm^{-1} to 1478 cm^{-1} (Supplementary Fig. 7b), providing further evidence for the presence of electrostatic interactions between the carboxyl groups of CA and the quaternary ammonium groups of QCS upon water exposure[24]. Additionally, Raman spectroscopy demonstrated that the benzene ring deformation peak shifted from 1612 cm^{-1} to 1615 cm^{-1} upon wetting (Supplementary Fig. 7c), which was attributed to the formation of cationic-π interactions between the catechol groups of CA and the amine groups of QCS[25,26]. Overall, the combined spectroscopic analyses demonstrated that water acts as a molecular trigger, facilitating the formation of multiple intermolecular interactions, including hydrogen bonding, electrostatic attraction, and cationic-π interactions between QCS and CA. These water-mediated interactions promote self-bonding between QCS@PVA and CA@PVA nanofibers, resulting in a structural transformation from a porous architecture to a compact, integrated network (Fig. 2c). This structural reorganization significantly enhances the nanofabric's barrier properties against water molecule penetration, establishing a robust water-resistant material system.

Water blocking study II: Wet tissue adhesion for preventing water seepage at the fabric/tissue interface

As demonstrated above, QCS@PVA/CA@PVA nanofabric can adhere to the glass. To investigate its adhesion properties on biological tissues, QCS@PVA/CA@PVA nanofabric was applied to various wet organs such as the heart, liver, spleen, lung, kidney, and small intestine. As shown in Fig. 3a, the fabric adhered securely to these biological tissues. Furthermore, when pressed onto the wet human wrist, QCS@PVA/CA@PVA nanofabric could tightly adhere to it and adapt to the bending and straightening motions without detachment (Fig. 3b). To quantitatively assess the adhesion behavior of QCS@PVA/CA@PVA nanofabric, its adhesion strength was measured using lap-shear tests with wet porcine organs (Fig. 3c). The adhesion strength of the QCS@PVA/CA@PVA nanofabric was 35 kPa for heart, 42 kPa for liver, 51 kPa for lung, 61 kPa for kidney, 32 kPa for muscle, and 21 kPa for porcine skin. Notably, the adhesion of the fabric to internal organs was superior to its adhesion to skin, especially in the case of the kidney. The differential adhesive performance of fabrics across various tissues is primarily attributed to tissue-specific variations. The surfaces of visceral tissues, such as kidneys, are generally smoother and moister than the skin. This provides a larger contact area and a more uniform interface for the adhesive material, thereby enhancing the adhesive force[27,28]. In contrast, the skin surface has a stratum corneum and tiny uneven structures, which may reduce the direct contact area between the material and the tissue. At the same time, the extracellular matrix of visceral tissues contains rich components such as collagen and glycosaminoglycans. These components can form strong intermolecular forces with the functional groups (such as hydroxyl groups, carboxyl groups, amino groups, etc.) in the adhesive material[27]. In contrast, the stratum corneum of the skin surface is mainly composed of hydrophobic keratin, which may limit the interaction between the adhesive material and the tissue. In addition, the surface energy of visceral tissues is usually higher, especially in a moist environment. This helps the adhesive material to form stronger intermolecular forces (such as hydrogen bonds, electrostatic interactions, etc.) with the tissue surface[28]. However, the stratum corneum of the skin surface has a lower surface energy, which may limit the interaction between the adhesive material and the skin. Based on the influence of these factors, our material exhibits tissue-dependent adhesive performance. These factors collectively influence the molecular interactions between the fabric and tissues, resulting in tissue-dependent adhesive performance. Furthermore, the adhesion strength (21-61 kPa) of the QCS@PVA/CA@PVA nanofabric on tissues exceeded that of commercial fibrin glue (~10 kPa). In contrast, the PVA, QCS@PVA, and CA@PVA nanofabrics showed poor tissue adhesion behavior, with adhesion strength of below 10 kPa. The adhesion strength of commercial hemostatic fabrics such as cotton gauze and Combat Gauze™ were too weak to provide measurable adhesion data. The microstructure of the interface between the QCS@PVA/CA@PVA nanofabric and porcine tissues was observed using SEM (Supplementary Fig. 8). Apart from the compact structure of the QCS@PVA/CA@PVA nanofabric, a tightly coherent interface was observed between the fabric and the tissue, suggesting strong interfacial adhesion. These above results demonstrated that QCS@PVA/CA@PVA nanofabric possessed excellent tissue adhesion. The wet tissue adhesion of the QCS@PVA/CA@PVA nanofabric is related to the following factors: (I) absorption of the interfacial water. When the porous QCS@PVA/CA@PVA nanofabric comes into contact with moist tissues, it rapidly absorbs interfacial water. This process serves a dual purpose: firstly, the elimination of interfacial water promotes direct contact between the fabric and the tissue surface, enhancing interfacial interactions[29]. Secondly, the absorbed water acts as an efficient plasticizer, permeating the nanofabric matrix and significantly increasing the mobility of polymer segments, particularly those of QCS and CA. This enhanced segmental mobility facilitates greater chain flexibility and deformation, allowing the polymer chains to achieve optimal conformation with the tissue substrate surface, thereby improving adhesion performance[30]. (II) Interfacial interaction. The functional groups (including hydroxyl, amine, carboxyl, and catechol moieties) on the nanofabric can engage in molecular interactions with complementary groups (amine, carboxyl, and sulfhydryl) on the tissue surface. These interactions, encompassing hydrogen bonding, electrostatic forces, and cation-π interactions, collectively confer tissue-adhesive properties to the QCS@PVA/CA@PVA nanofabric[31–33].

In addition, debonding-on-demand is a crucial factor to consider when using hemostatic dressings, as it ensures that the removal of the dressing does not cause any further harm to the wound. Fortunately, debonding of the QCS@PVA/CA@PVA nanofabric can be achieved by the addition of 0.9% NaCl solution at the interface between QCS@PVA/CA@PVA nanofabric and tissue (Supplementary Fig. 9, Supplementary Movie 2). NaCl solution can destroy the electrostatic interaction[34].

Based on those above results, we find that the porous QCS@PVA/CA@PVA nanofabric has the ability to self-seal upon contact with water, forming a compact barrier that effectively inhibits water penetration (Fig. 3d). Additionally, this compact barrier can firmly adhere to tissue, which is beneficial in preventing water seepage at the fabric/tissue interface. These characteristics contribute to the sealing wound ability of the QCS@PVA/CA@PVA nanofabric. To explore the sealing performance of the QCS@PVA/CA@PVA nanofabric, a porcine small intestine was used as a model. The small intestine was filled with orange PBS solution stained with methyl orange. As shown in Fig. 3e and Supplementary Movie 3, a wound of 1.25 mm diameter was made

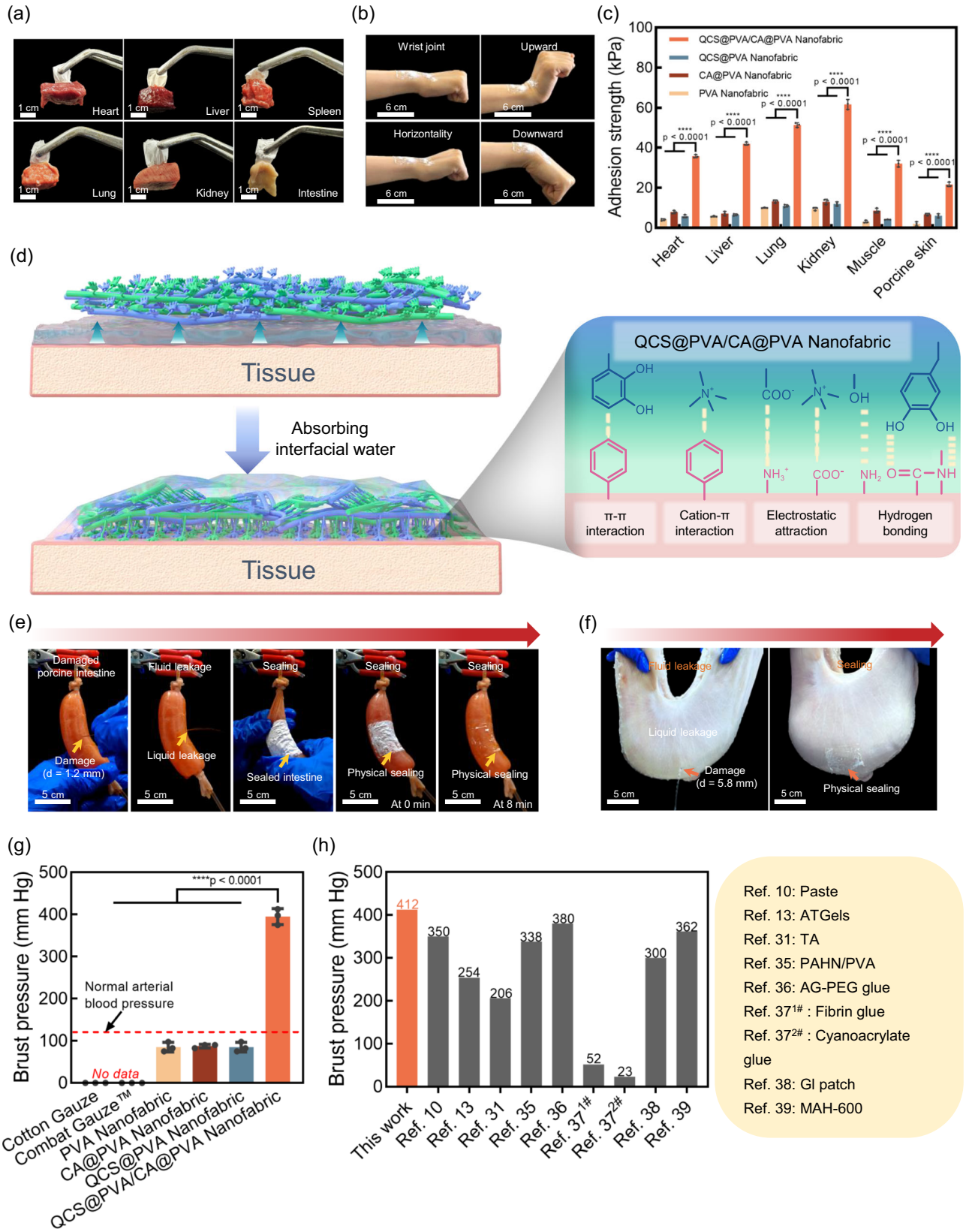

on the small intestine using a syringe needle, followed by the placement of one layer of QCS@PVA/CA@PVA nanofabric with a thickness of 0.2 μm on the wound. It was observed that there was no fluid leakage around the fabric. Additionally, no fluid permeated through the QCS@PVA/CA@PVA nanofabric. These findings highlight the effective sealing performance of the QCS@PVA/CA@PVA nanofabric, which was further confirmed through a seal test conducted on a damaged stomach (Fig. 3f). To investigate the capacity of withstanding blood pressure of QCS@PVA/CA@PVA nanofabric, burst pressure was measured with a home-made device. QCS@PVA/CA@PVA nanofabric shows a remarkably higher average burst pressure (412 mm Hg) than PVA nanofabric (85 mm Hg), QCS@PVA nanofabric (87 mm Hg), and

Fig. 3 | Wet tissue adhesion for preventing water seepage at the fabric/tissue interface. a Images of the adhesion behavior of QCS@PVA/CA@PVA nanofabric on various pig organs (heart, liver, spleen, lung, kidney, and intestine). **b** Digital photos of QCS@PVA/CA@PVA nanofabric adhering to the wet human wrist. **c** Adhesion strength of PVA nanofabric, QCS@PVA nanofabric, CA@PVA nanofabric, and QCS@PVA/CA@PVA nanofabric on various pig organs. **d** Scheme representation of the tissue adhesion mechanism of QCS@PVA/CA@PVA nanofabric. **e**, **f** In vitro wound sealing of pig's intestine and stomach using QCS@PVA/CA@PVA nanofabric. **g** Bursting pressure of PVA nanofabric, QCS@PVA nanofabric, CA@PVA nanofabric, and QCS@PVA/CA@PVA nanofabric on porcine skin. **h** Comparative burst pressure of QCS@PVA/CA@PVA nanofabric and some recently reported wet adhesives[10,13,31,42–46]. Data are presented as mean ± SD ($n = 3$ independent samples). Statistical comparisons for **c**, **g** were performed using two-tailed Student's t tests. ns = not significant, $^{*}p < 0.05$, $^{**}p < 0.01$, $^{***}p < 0.001$, $^{****}p < 0.000$. In **a**, **b**, **e**, **f**, images from one representative experiment of three independent experiments are presented.

CA@PVA nanofabric (90 mm Hg) (Fig. 3g and Supplementary Movie 4). Notably, the remarkably high burst pressure achieved by the QCS@PVA/CA@PVA nanofabric significantly exceeded normal blood pressure (120 mmHg) and outperformed commercial wet-tissue adhesives such as fibrin and cyanoacrylate glues, as well as recently reported wet adhesives (Fig. 3h).

Hemocompatibility, cytocompatibility, biodegradation, and antibacterial activity

The main components of the QCS@PVA/CA@PVA nanofabric are chitosan, alginate, and PVA. These materials are commonly used as promising biomaterials because of their exceptional biocompatibility and biodegradability. Therefore, it is expected that QCS@PVA/CA@PVA nanofabric would exhibit biocompatibility and biodegradability. To validate this assumption, the hemocompatibility and cytocompatibility of QCS@PVA/CA@PVA nanofabric were assessed. Figure 4a shows the hemocompatibility assessment of cotton gauze, Combat Gauze™, QCS@PVA/CA@PVA nanofabric. With increasing concentrations of QCS@PVA/CA@PVA nanofabric from 0.5 mg/mL to 4 mg/mL, there was no noticeable change in the color of the supernatant, which remained colorless similar to the PBS group. The hemolysis ratios of QCS@PVA/CA@PVA nanofabric were lower than those of cotton gauze and Combat Gauze™ (Fig. 4b), indicating favorable hemocompatibility. Figure 4c shows the cytocompatibility assessment of cotton gauze, Combat Gauze™, QCS@PVA/CA@PVA nanofabric. The majority of cells in QCS@PVA/CA@PVA exhibited a spindle green color, similar to the blank group, and the change in cell count was consistent with the results of the cell viability test (Fig. 4d). The cell viability of QCS@PVA/CA@PVA nanofabric was nearly 100%, indicating that it is non-toxic to cells. The results from the cytotoxicity evaluation and hemolysis ratio measurement confirm the biosafety of QCS@PVA/CA@PVA nanofabric, making it a promising material for hemostatic applications.

Degradation is an important index for hemostatic materials, as it can prevent the need for secondary surgical removal of residual materials following hemostasis. The QCS@PVA/CA@PVA nanofabrics were subcutaneously implanted into rats to investigate their in vivo biodegradation. As illustrated in Fig. 4e, f, a significant increase in degradation (ca.75%) was observed after 7 days of implantation, with almost no residual scaffolds remaining after 14 days. This finding suggests that the QCS@PVA/CA@PVA nanofabrics exhibit excellent biodegradability. Furthermore, the anti-inflammatory properties of the QCS@PVA/CA@PVA nanofabric were assessed through H&E staining and IL-6 expression analysis. H&E staining revealed a significant accumulation of inflammatory cells at the tissue interfaces in direct contact with the QCS@PVA/CA@PVA nanofabrics one day post-implantation (Fig. 4g). Concurrently, high levels of IL-6 expression were observed, indicative of mild inflammation triggered by a typical foreign-body reaction (Fig. 4h). Importantly, the fluorescence intensity of IL-6 progressively declined, and the inflammation subsided as the QCS@PVA/CA@PVA nanofabrics degraded. This reduction suggests that the material exhibits excellent biocompatibility in vivo, allowing the immune system to adapt to its presence and ultimately cease the production of an inflammatory response. The exceptional biocompatibility and biodegradability of the QCS@PVA/CA@PVA nanofabric can be attributed to its primary components, namely chitosan, sodium alginate, and PVA, all of which are well-known for their favorable biological properties. According to the literature, the degradation pathways of these components in the human body are as follows: Lysozymes can cleave the β-1,4-glycosidic bonds in chitosan, breaking it down into glucosamine, which subsequently enters glycolysis and the tricarboxylic acid cycle, ultimately participating in energy metabolism[35]. For alginate, alginate lyase specifically targets the glycosidic bonds between mannuronic acid and guluronic acid, progressively degrading sodium alginate into smaller oligosaccharide fragments. These fragments can be absorbed through the intestinal wall or excreted in feces[36,37]. As for PVA, its degradation primarily relies on hydrolysis and excretion through the excretory system, with macrophages encapsulating PVA via phagocytosis to facilitate its breakdown[38].

Skin sensitization represents a hypersensitivity reaction that typically develops following prolonged or repeated exposure of the immune system to chemical substances. The sensitization potential of the QCS@PVA/CA@PVA nanofabric was evaluated using guinea pigs. The results are presented in Supplementary Fig. 10 and Supplementary Table 1. Physiological saline (0.9% NaCl) and 10% sodium dodecyl sulfate (SDS) served as negative and positive controls, respectively. Notably, guinea pigs exposed to the QCS@PVA/CA@PVA nanofabric showed no clinical evidence of skin irritation, with the absence of both erythema and edema throughout the observation period. These observations were comparable to those recorded in the negative control group. The experimental data conclusively demonstrate that the QCS@PVA/CA@PVA nanofabric lacks sensitizing potential and displays outstanding skin compatibility, suggesting its suitability for biomedical applications requiring prolonged dermal contact.

Moist wounds with low oxygen levels can promote bacterial growth and increase the risk of inflammation. Therefore, antibacterial properties are important for hemostatic materials. The antibacterial activity of QCS@PVA/CA@PVA nanofabric was evaluated using a colony-forming unit assay (CFU) with Gram-positive *S. aureus* and Gram-negative *E. coli*. In Fig. 4i, the colony-forming units of *E. coli* and *S. aureus* were compared after incubation with cotton gauze, Combat Gauze™, and QCS@PVA/CA@PVA. A significant number of bacteria were observed in the cotton gauze group, with antibacterial ratios as low as 7% for *E. coli* and 18% for *S. aureus* (Fig. 4j, k), indicating a weak antibacterial effect. While the Combat Gauze™ exhibited slightly better antibacterial characteristics than cotton gauze, the antibacterial ratios were only 30% for *E. coli* and 28% for *S. aureus*, suggesting a limited antibacterial effect. In contrast, the QCS@PVA/CA@PVA nanofabric group showed almost no bacteria, indicating effective bacterial elimination by the QCS@PVA/CA@PVA nanofabric. SEM was utilized to analyze the morphological alterations of *S. aureus* and *E. coli* following treatment with the hemostatic fabric. As depicted in Fig. 4l, similar to the control group, the cotton gauze group exhibited rod-shaped *E. coli* and cocci-shaped *S. aureus*. In the Combat Gauze™ group, the majority of the bacteria maintained morphology, with both *S. aureus* and *E. coli* surfaces displaying smooth textures. Only a small number of bacteria appeared depressed and deformed. Conversely, nearly all bacteria in the QCS@PVA/CA@PVA nanofabric

https://doi.org/10.1038/s41467-025-60244-z

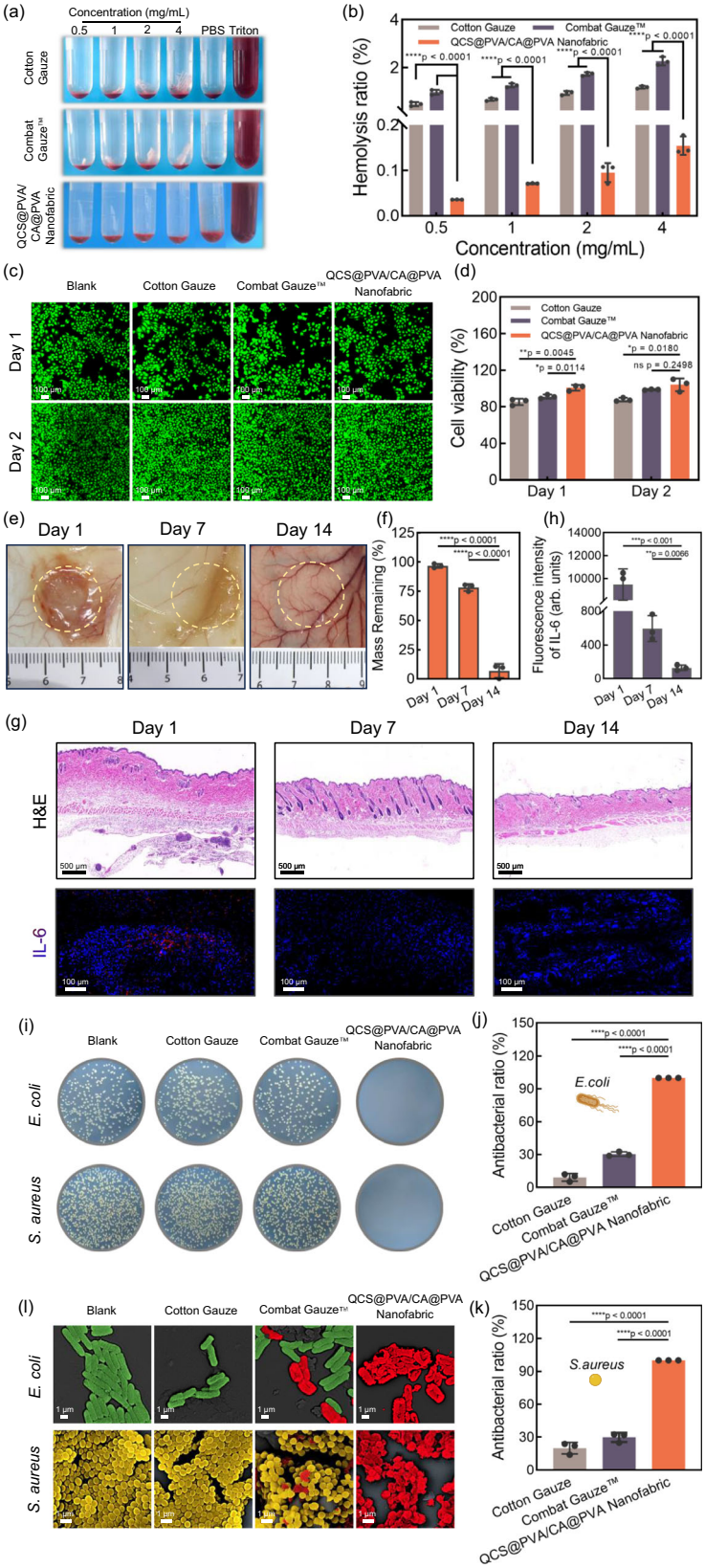

group were observed to be collapsed and broken. These results indicated that QCS@PVA/CA@PVA nanofabric displayed excellent antibacterial activity. Moreover, the antibacterial activity QCS@PVA/CA@PVA nanofabric exhibits superior antibacterial activity compared to the commercial antibacterial hemostatic chitoGauze®, as shown in Supplementary Fig. 11. The remarkable antibacterial activity of QCS@PVA/CA@PVA nanofabric is mainly due to the presence of catechol groups and quaternary ammonium groups. Catechol groups exhibit a high binding affinity to proteins on bacterial membranes, while quaternary ammonium groups can adhere to the negatively charged bacterial membrane. This interaction disrupts normal bacterial growth, ultimately functions as a bacteriostatic agent[39,40].

Fig. 4 | Hemocompatibility, cytocompatibility, biodegradability, and antibacterial activity of QCS@PVA/CA@PVA nanofabric. a Photographs of the hemolytic activity assay and **b** hemolysis ratio of cotton gauze, Combat Gauze™, and QCS@PVA/CA@PVA nanofabric. **c** Fluorescence images of Human umbilical vein endothelial cells and (**d**) cell viability after 24 h and 48 h incubation with cotton gauze, Combat Gauze™, and QCS@PVA/CA@PVA nanofabric. **e** Representative images and (**f**) mass remaining of QCS@PVA/CA@PVA nanofabric following subcutaneous implantation into rats at different time points. Yellow dashed lines represent the degradation process of QCS@PVA/CA@PVA nanofabric in vivo. **g** H&E staining images and immunohistochemistry staining of IL-6 for skin tissues surrounding QCS@PVA/CA@PVA nanofabric at corresponding time points. **h** Statistical analysis of IL-6 expression. **i** Photographs of colony-forming units of *E. coli* and *S. aureus* after 24 h coculture with cotton gauze, Combat Gauze™, and QCS@PVA/CA@PVA nanofabric. Antibacterial ratio of each hemostatic fabric toward **j** *E. coli* and **k** *S. aureus*. **l** SEM images of *E. coli* and *S. aureus* after 24 h coculture with cotton gauze, Combat Gauze™, and QCS@PVA/CA@PVA nanofabric. Data are presented as mean ± SD ($n = 3$ independent samples). Statistical comparisons for (**b**, d, **f**, h, **j**, k) were performed using two-tailed Student's *t* tests. ns = not significant, $^{*}p < 0.05$; $^{**}p < 0.01$, $^{***}p < 0.001$, $^{****}p < 0.000$. In **a**, **c**, i, images from one representative experiment of three independent experiments are presented. In **l**, the representative SEM images are shown (at least three images were taken for each sample). The representative images in **e** and **g** are shown from three independent mice.

Encapsulation of the blood components to form a robust clot

The in vitro blood clotting test was performed by adding 50 µL of anticoagulant blood to the hemostatic fabrics, followed by injecting PBS at specified intervals. Figure 5a illustrates the blood coagulation status of fabrics after 30 s of blood contact. Obviously, blood stain on the cotton gauze could be easily removed with PBS, turning the eluent red. This indicates that the blood on the cotton gauze had not solidified within the initial 30 s of contact, but required ca. 384 s to fully clot (Fig. 5b). A similar trend was seen in the Combat Gauze™ group, with the blood clotting time of 375 s. Upon contact with blood, the PVA nanofabric shrank and enveloped the blood. However, the blood was able to be released when PBS was injected. The clotting time of the PVA nanofabric group was up to 356 s. While both QCS@PVA nanofabric and CA@PVA nanofabric demonstrated slightly better coagulation abilities compared to the PVA nanofabric, as evidenced by lighter eluent color and reduced clotting times of 321 s and 322 s, respectively. However, the eluent in these groups still exhibited a pink color, indicating some hemoglobin could still diffuse into PBS. In contrast, the QCS@PVA/CA@PVA nanofabric group had almost colorless eluent, suggesting that blood could be fully clotted by QCS@PVA/CA@PVA nanofabric within 30 s. Furthermore, even after vigorous shaking for 10 min, the blood clot remained stable on the QCS@PVA/CA@PVA without breaking apart (Supplementary Movie 5). These results demonstrated that QCS@PVA/CA@PVA nanofabric can rapidly initiate blood clotting and generate a robust thrombus. To quantitatively assess the blood clotting ability of these hemostatic fabrics, the BCI value was measured. This value is determined by the absorbance of residual hemoglobin that is not part of the blood coagulation process. A lower BCI value indicates a higher coagulation ability. As illustrated in Fig. 5c, QCS@PVA/CA@PVA nanofabric exhibited the lowest BCI value of 8% compared to other hemostatic fabrics such as cotton gauze (86%), Combat Gauze™ (82%), PVA nanofabric (72%), CA@PVA nanofabric (61%), and QCS@PVA nanofabric (55%), further confirming its superior procoagulant properties. Platelets and erythrocytes have important roles in blood coagulation, and we evaluated their adhesion to hemostatic fabrics. Kaolin particles tended to detach easily from Combat Gauze™ into PBS, causing interference with the test and hindering the accuracy of data collection. Therefore, we conducted a comparison between QCS@PVA/CA@PVA nanofabric, cotton gauze, PVA nanofabric, CA@PVA nanofabric, and QCS@PVA nanofabric in this study. The results of this comparison are illustrated in Fig. 5d, e. Cotton gauze exhibited low adhesion ratios of only 20% and 6% for platelets and erythrocytes, respectively. PVA nanofabric group also showed poor adhesion for platelets (14%) and erythrocytes (12%). CA@PVA nanofabric demonstrated higher platelet adhesion ratio (18%) and erythrocyte adhesion ratio (19%) compared to the PVA group, indicating that CA facilitated adhesion, likely due to the presence of catechol groups. Similarly, QCS@PVA exhibited increased platelet adhesion ratio (20%) and erythrocyte adhesion ratio (20%), suggesting that QCS can promote the adhesion of platelets and erythrocytes, attributed to the interaction between amino/quaternary ammonium groups on QCS and platelets/erythrocytes. Remarkably, the QCS@PVA/CA@PVA showed remarkably high platelet adhesion ratio (89%) and erythrocyte adhesion ratio (76%), significantly surpassing the individual QCS@PVA nanofabric and CA@PVA nanofabric. The adhesion behavior of platelets/erythrocytes was also observed by SEM. As shown in Fig. 5f, sporadic erythrocytes and platelets were found adhered to the surface of cotton gauze fibers, similar to what was observed on Combat Gauze™. In the PVA group, only a limited number of erythrocytes and platelets were distributed on the fibrous network surface. A higher presence of erythrocytes and platelets was noted in QCS@PVA and CA@PVA compared to the PVA group. Unlike the fibrous structure seen in PVA nanofabric, CA@PVA nanofabric, and QCS@PVA nanofabric, QCS@PVA/CA@PVA nanofabric displayed a dense membrane with erythrocytes and platelets encapsulated within it, implying that the water-induced in situ self-bonding process of QCS@PVA/CA@PVA nanofabric significantly contributes to blood coagulation. As illustrated in Fig. 5g, upon contact with blood, the QCS@PVA nanofibers and CA@PVA nanofibers absorbed the plasma and quickly in situ bonded with each other, forming a dense structure. This process resulted in the encapsulation of blood components within a robust membrane, facilitating the formation of a strong and stable clot.

In vivo hemostasis in rat and pig models

The in vivo hemostatic performance of these hemostatic fabrics was evaluated by femoral artery and rat liver injury models (Fig. 6a). The hemostasis process in the rat femoral artery injury model using various hemostats is depicted in Fig. 6b. Upon unloading the compression, blood rapidly saturated the cotton gauze, gradually seeping through and eventually leaking out, leading to a considerable blood loss of ca. 947.37 mg and a long hemostatic time of ca. 235.67 s (Fig. 6c, d). The hemostatic behavior of Combat Gauze™ is similar to that of cotton gauze, with blood swiftly saturating the entire Combat Gauze™ and permeating through. However, the presence of procoagulant kaolin particles in Combat Gauze™ resulted in a slightly lower amount of blood seepage compared to cotton gauze, decreasing from ca. 947.37 mg to ca. 703.33 mg. The hemostatic time reduced from ca. 235.67 s to ca. 147.42 s. The blood flow direction in the PVA nanofabric group differed from that of the cotton gauze group and Combat Gauze™ group. Upon contact with blood, the PVA nanofabric gradually became transparent with blood seeping out slowly. The penetration rate was slower than that of the gauze group, which can be attributed to the smaller cavities within the PVA nanofabric compared to cotton gauze and Combat Gauze™, limiting the longitudinal blood flow. Nevertheless, a considerable amount of blood seeped out from the seam of the PVA nanofabric and tissue surface, leading to significant blood loss. The hemostatic efficiency of PVA nanofabric was comparable to that of cotton gauze, with blood loss and hemostatic time of up to ca. 929.27 mg and ca. 294.67 s, respectively. Similarly, both CA@PVA nanofabric and QCS@PVA nanofabric demonstrated the ability to reduce the rate of blood penetration through the fabric, but could not stop blood from flowing between the seam of the fabric and tissue. The blood loss of CA@PVA nanofabric and QCS@PVA

https://doi.org/10.1038/s41467-025-60244-z

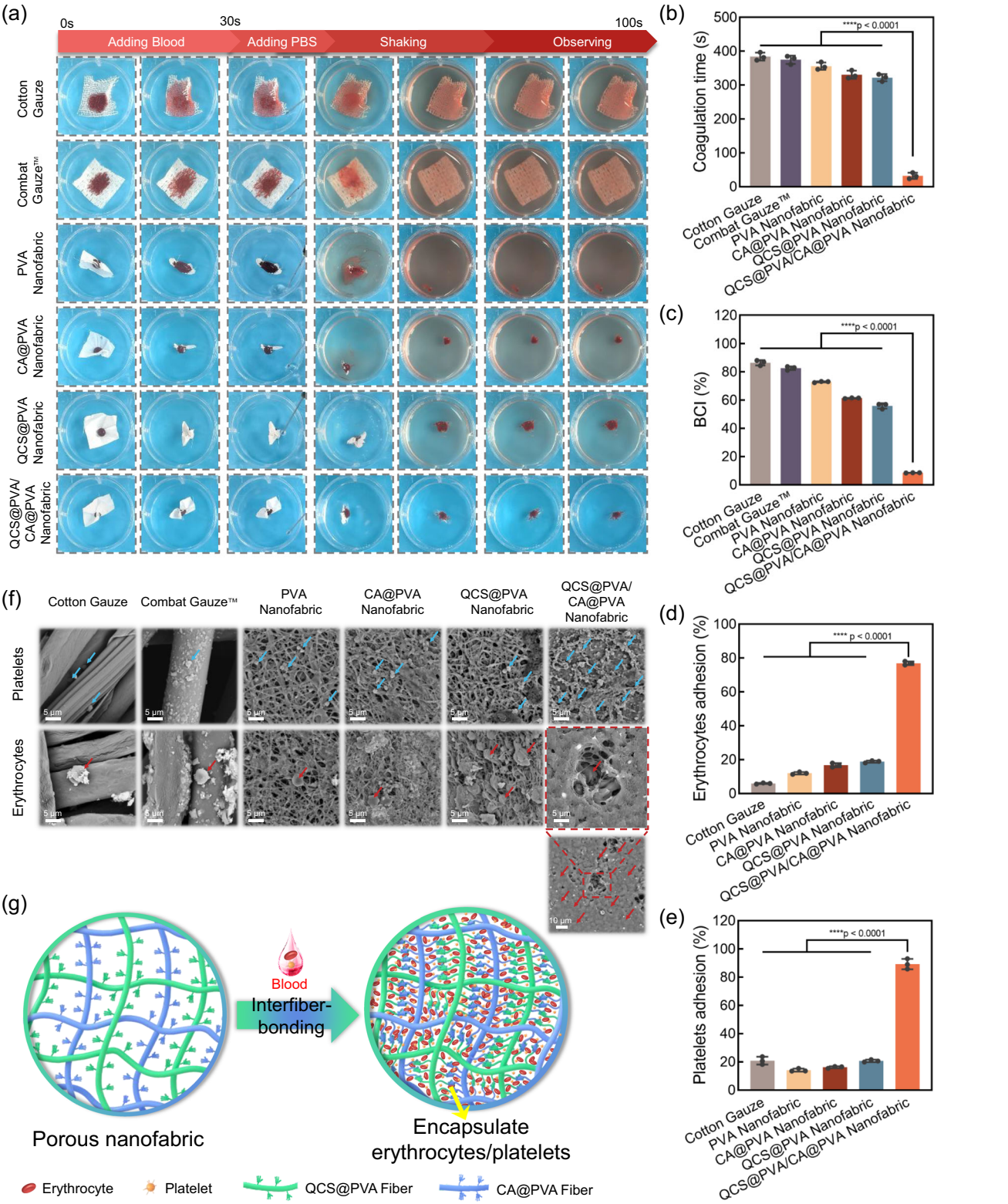

Fig. 5 | In vitro coagulation behavior of QCS@PVA/CA@PVA nanofabric. **a** Photographs of the blood coagulation status of cotton gauze, Combat Gauze™, PVA nanofabric, CA@PVA nanofabric, QCS@PVA nanofabric, and QCS@PVA/CA@PVA nanofabric after 30 s of blood contact. **b** Coagulation time and **c** BCI value of cotton gauze, Combat Gauze™, PVA nanofabric, CA@PVA nanofabric, QCS@PVA nanofabric, and QCS@PVA/CA@PVA nanofabric. The percentage of **d** platelets and **e** erythrocytes adhesion on these hemostatic fabrics. **f** SEM images of platelets and erythrocytes adhesion on various hemostatic fabrics. **g** Clotting mechanism of QCS@PVA/CA@PVA nanofabric. Data are presented as mean ± SD ($n = 3$ independent samples). Statistical comparisons for (**b**, **c**, **e**, **f**) were performed using two-tailed Student's t tests. ****$p < 0.000$. In a, images from one representative experiment of three independent experiments are presented. In d, the representative SEM images are shown (at least three images were taken for each sample). (Blue arrow: platelets; red arrow: erythrocytes; yellow arrow: captured blood cells).

https://doi.org/10.1038/s41467-025-60244-z

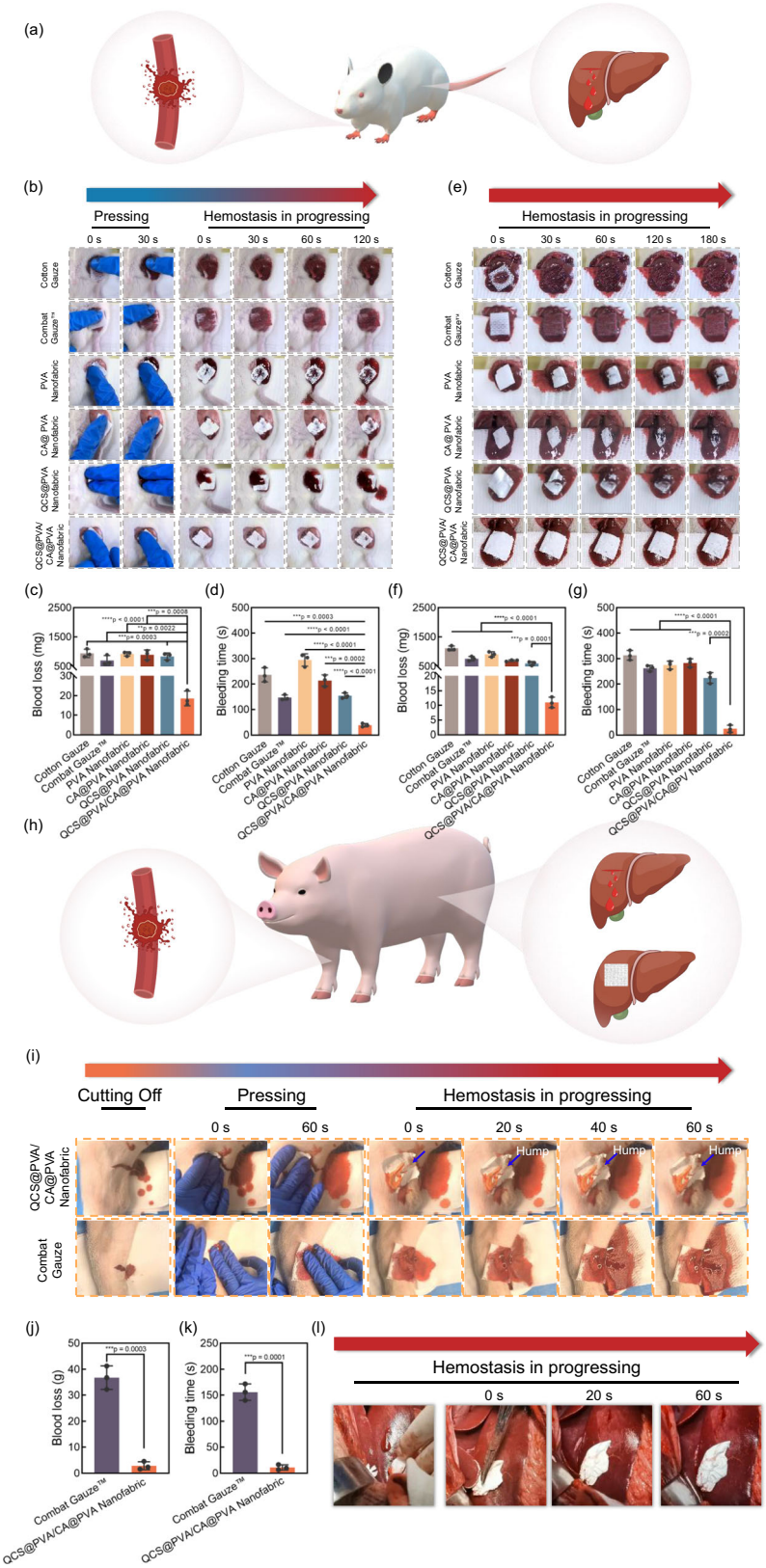

nanofabric was ca. 896.97 mg and ca. 841.73 mg, respectively. In contrast, the outer surface of QCS@PVA/CA@PVA nanofabric remained dry, and no blood spread around the wound, suggesting its potential as a reliable physical barrier for controlling bleeding effectively. The blood loss of QCS@PVA/CA@PVA nanofabric significantly decreased to 18.56 mg, which was ca. 1.95% and 2.68% of cotton gauze and Combat Gauze™, respectively. Additionally, the bleeding time for QCS@PVA/CA@PVA nanofabric was only 38 s. The hemostatic performance of QCS@PVA/CA@PVA nanofabric in a non-compressible wound was evaluated by using the rat liver laceration model. As shown in Fig. 6e, their behaviors of blood diffusion, flow at the seam of fabric/tissue were similar to the hemostasis on the rat femoral artery injury

Fig. 6 | In vivo hemostatic efficiency of QCS@PVA/CA@PVA nanofabric. **a** Scheme representation of the rat femoral artery trauma model and liver trauma model. **b** Photographs of hemostasis progress, **c** blood loss, **d** bleeding time of cotton gauze, Combat Gauze™, PVA nanofabric, CA@PVA nanofabric, QCS@PVA nanofabric, and QCS@PVA/CA@PVA nanofabric in the rat femoral artery trauma model. **e** Photographs of hemostasis progress, **f** blood loss, **g** bleeding time of cotton gauze, Combat Gauze™, PVA nanofabric, CA@PVA nanofabric, QCS@PVA nanofabric, and QCS@PVA/CA@PVA nanofabric in the rat liver trauma model. **h** Scheme representation of the pig femoral artery trauma model and liver trauma model. **i** Photographs of hemostasis progress, **j** blood loss, and **k** bleeding time of Combat Gauze™ and QCS@PVA/CA@PVA nanofabric in the pig femoral artery trauma model. **l** Photographs of hemostasis progress of QCS@PVA/CA@PVA nanofabric in the pig liver trauma model. Data are presented as mean ± SD ($n = 3$ independent samples). Statistical comparisons for (**c**–**g**, j, **k**) were performed using two-tailed Student's t tests. ns = not significant, $^{*}p < 0.05$, $^{**}p < 0.01$, $^{***}p < 0.001$, $^{****}p < 0.000$. The representative images in **b** and e are shown from three independent mice. The representative images in **i** and **l** are shown from three independent pigs. (Blue arrow: blocked blood pressure).

model. Obviously, the hemostatic efficacy of QCS@PVA/CA@PVA nanofabric was significantly better than the other groups, including cotton gauze, Combat Gauze™, PVA nanofabric, CA@PVA nanofabric, and QCS@PVA nanofabric. Blood loss measurements for cotton gauze, Combat Gauze™, QCS@PVA nanofabric, CA@PVA nanofabric, and QCS@PVA/CA@PVA nanofabric were ca. 1119.90 mg, ca. 764.23 mg, ca. 912.47 mg, ca. 697.61 mg, ca. 603.74 mg, and 11.33 mg, respectively (Fig. 6f). In terms of hemostatic time, cotton gauze, Combat Gauze™, QCS@PVA nanofabric, CA@PVA nanofabric, and QCS@PVA/CA@PVA nanofabric took approximately 313.33 s, 261.67 s, 274.33 s, 284.57 s, 223.33 s, and 24.12 s, respectively (Fig. 6g). Notably, compared to Combat Gauze™, QCS@PVA/CA@PVA nanofabric showed a 90.78% reduction in hemostatic time and a 98.51% reduction in blood loss. The results of in vivo rat hemostatic measurements clearly demonstrate the effectiveness of QCS@PVA/CA@PVA nanofabric in treating both arterial injuries and noncompressible liver puncture wounds. Its hemostatic performance was found to be superior to that of commercial hemostatic fabric, including cotton gauze and Combat Gauze™.

To further evaluate the hemostatic effectiveness of QCS@PVA/CA@PVA nanofabric on severe bleeding wounds, we utilized the pig femoral artery injury model and liver trauma model as depicted in Fig. 6h. The process of hemostasis on the pig femoral artery injury model was illustrated in Fig. 6i and Supplementary Movie 6. Following the incision of the pig's femoral artery, a significant amount of blood was observed to flow out. Promptly, we applied QCS@PVA/CA@PVA nanofabric to the wound and compressed for 60 s. Upon releasing the compression, we were surprised to observe a hump in the middle of QCS@PVA/CA@PVA nanofabric, due to blood accumulation. Despite the blood pressure, the hump remained intact over time, with QCS@PVA/CA@PVA nanofabric still firmly adhered to the pig's skin. Notably, the blood-stained area on the gauze pad under the pig's leg did not expand, implying that the bleeding was successfully controlled by QCS@PVA/CA@PVA nanofabric. Conversely, the bleeding was not yet controlled by Combat Gauze™, as blood continued to flow out and permeate the gauze placed under the pig's leg. The blood loss of Combat Gauze™ was up to ca. 36.85 g, while the blood loss of QCS@PVA/CA@PVA nanofabric was only ca. 2.91 g (Fig. 6l). The results of the pig femoral artery injury further justify that QCS@PVA/CA@PVA had excellent hemostatic efficacy for severe bleeding wounds. In addition, the QCS@PVA/CA@PVA nanofabric demonstrated rapid hemostatic efficacy on a bleeding pig liver injury (Fig. 6l, k and Supplementary Movie 7). Upon placement of the QCS@PVA/CA@PVA nanofabric on the wound, it tightly adhered to the liver surface, effectively stopping the bleeding.

Supplementary Fig. 12 shows the microstructure of the QCS@PVA/CA@PVA nanofabric and the formed thrombus following hemostasis in the rat femoral artery trauma model. It is evident that the porous QCS@PVA/CA@PVA nanofabric developed a dense membrane post-hemostasis. Notably, no thrombus was detected on the surface of the QCS@PVA/CA@PVA nanofabric; however, a significant accumulation of erythrocytes and platelets was observed beneath it. This finding indicates that the blood-triggered wound sealing mechanism of the QCS@PVA/CA@PVA nanofabric effectively obstructs blood flow and intercepts erythrocytes and platelets. The accumulation of these

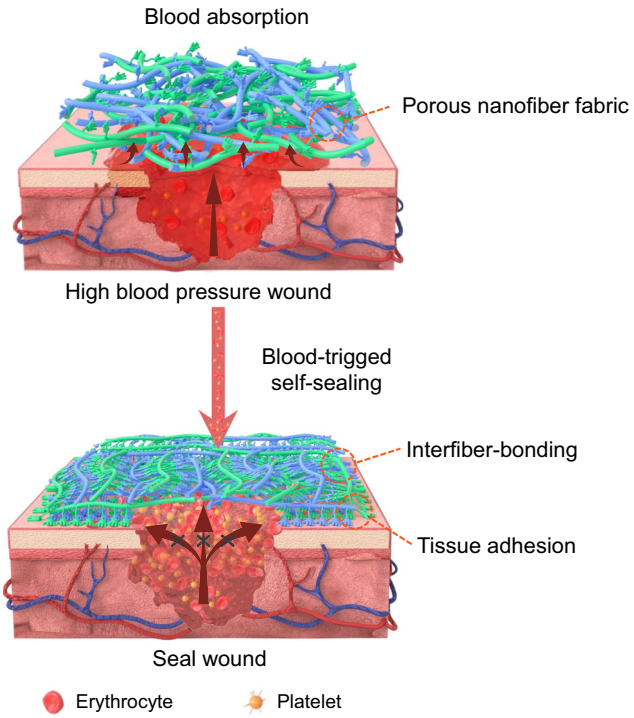

Fig. 7 | Schematic illustration of hemostatic mechanisms of QCS@PVA/CA@PVA nanofabric. The porous QCS@PVA/CA@PVA nanofabric absorbs plasma and rapidly self-seals into a compact barrier via interfiber-bonding, effectively preventing blood from penetrating longitudinally through the fabric. The QCS@PVA/CA@PVA nanofabric can strongly adhere to wound tissue, impeding blood seepage at the fabric/tissue interface.

trapped erythrocytes and platelets at the wound site contributes to the formation of blood clots, thereby further enhancing blood control.

Based on the results of in vivo hemostasis experiments, a proposed hemostatic mechanism for the QCS@PVA/CA@PVA nanofabric is illustrated in Fig. 7. Upon contact with blood, the porous QCS@PVA/CA@PVA nanofabric absorbs plasma and rapidly self-seals into a compact barrier via interfiber-bonding, effectively preventing blood from penetrating longitudinally through the fabric. Additionally, the QCS@PVA/CA@PVA nanofabric can strongly adhere to wound tissue, impeding blood seepage at the fabric/tissue interface. The combined effects of interfiber bonding and superior tissue adhesion enable the QCS@PVA/CA@PVA nanofabric to effectively seal wounds to control blood flow. Erythrocytes and platelets are trapped by the QCS@PVA/CA@PVA nanofabric and aggregate at the wound site, facilitating the formation of blood clots and further enhancing blood control.

Wound Healing

Bleeding typically occurs as a result of tissue damage, and once hemostasis is achieved, tissue repair becomes necessary. In this study, a rat model of full-thickness skin defect repair was used to assess the effectiveness of QCS@PVA/CA@PVA nanofabric as a wound dressing in facilitating wound healing. Figure 8a illustrates the wound healing

process of various dressing samples, including Tegaderm™, Combat Gauze™, cotton gauze, and QCS@PVA/CA@PVA nanofabric. The wound areas of all groups decreased over time. By the 7th day, the visible scar was evident in the QCS@PVA/CA@PVA nanofabric group, while suppuration was observed in the Tegaderm™ and Combat Gauze™ groups. By the 11th day, the wound has already closed in the QCS@PVA/CA@PVA nanofabric group with a healing ratio of 98%, whereas the other groups still had unclosed wounds or residual scars (Fig. 8a, b), with healing rates of only 63%, 78%, and 81% for Tegaderm™, Combat Gauze™, and cotton gauze, respectively (Fig. 8c). These findings suggest that the QCS@PVA/CA@PVA nanofabric group exhibited the fastest rate of healing. The H&E, CD31 immunoffuorescent staining, as well as Masson trichrome staining, were used to investigate skin regeneration. As shown in Fig. 8d, QCS@PVA/CA@PVA nanofabric group exhibited a higher presence of fibroblasts in tissue sections stained by H&E compared to other groups. Immunofluorescent staining for CD31 revealed that the QCS@PVA/CA@PVA nanofabric group exhibited significantly higher levels of CD31 expression compared to the Tegaderm™, Combat Gauze™, and cotton gauze groups at day 7 (Fig. 8d and Supplementary Fig. 13). However, by day 14, the CD31 expression level in the QCS@PVA/CA@PVA nanofabric group markedly decreased, indicating that the newly formed tissue was transitioning into a mature phase. This shift suggests that the tissue had progressed from an active repair state to a more stable, steady state. In contrast, the Tegaderm™, Combat Gauze™, and cotton gauze groups still exhibited sustained CD31 expression by day 14. These findings demonstrate that the QCS@PVA/CA@PVA nanofabric possesses an ability to promote angiogenesis during wound healing. Additionally, the regenerated epithelial tissue in QCS@PVA/CA@PVA group appeared to be thicker than the cotton groups. The analysis of Masson's trichrome staining indicated that the QCS@PVA/CA@PVA group had a higher collagen volume compared to the Tegaderm™, Combat Gauze™, and cotton gauze groups, suggesting that QCS@PVA/CA@PVA nanofabric can promote collagen production and deposition during the proliferative stage of wound healing. These results highlight the promising wound healing performance of the QCS@PVA/CA@PVA nanofabric.

Discussion

In this work, we prepared a hemostatic nanofiber composed of anionic and cationic nanofibers with a core-shell structure, created through a double-coaxial electrospinning technique. The porous QCS@PVA/CA@PVA nanofabric demonstrated excellent air permeability comparable to cotton gauze and Combat Gauze™. Additionally, it exhibited good toughness and flexibility, with a tensile stress of 1.85 MPa and a strain of 162%, making it suitable for easy wound dressing. Upon contact with the blood, the porous QCS@PVA/CA@PVA nanofabric could absorb the blood and self-seal into a compact barrier by interfiber-bonding. This compact barrier can effectively prevent blood penetration. Furthermore, the hemostatic nanofiber fabric could strongly adhere to tissue. The adhesion strength (21 ~ 61 kPa) of the QCS@PVA/CA@PVA nanofabric on tissues exceeded that of commercial fibrin glue (~10 kPa). Such strong interaction between QCS@PVA/CA@PVA nanofabric and tissue can prevent water seepage at the fabric/tissue interface. Due to the synergistic effect of interfiber bonding and superior tissue adhesion, the QCS@PVA/CA@PVA nanofabric exhibits rapidly and effectively seals the damaged small intestine and stomach. QCS@PVA/CA@PVA nanofabric displayed a high burst pressure (412 mm Hg) exceeding normal blood pressure (120 mmHg). In vitro coagulation experiments demonstrated that the QCS@PVA/CA@PVA nanofabric can encapsulate blood components, leading to the formation of a strong clot, attributed to its water-triggered interfiber bonding. In vivo hemostatic experiments demonstrate that QCS@PVA/CA@PVA nanofabric possessed excellent wound sealing abilities across various injury models, such as rat femoral artery injury, rat liver laceration, pig femoral artery injury, and pig liver laceration. The hemostatic properties of this fabric surpass those of commercial hemostatic fabric including cotton gauze and Combat Gauze™. Particularly, the blood loss from QCS@PVA/CA@PVA nanofabric was approximately 8% of that from Combat Gauze™ in the pig femoral artery injury. The components of QCS@PVA/CA@PVA nanofabric, which include chitosan, PVA, and alginate, are well-known biomaterials known for their excellent biocompatibility and biodegradability. As a result, QCS@PVA/CA@PVA nanofabric exhibits outstanding hemocompatibility and cytocompatibility. Notably, this nanofabric also exhibits excellent biodegradability, eliminating the need for removal from the body after hemostasis, thereby reducing the risk of secondary wound injury and re-bleeding. The presence of catechol groups and quaternary ammonium groups in QCS@PVA/CA@PVA nanofabric resulted in antibacterial activity against *E. coli* and *S. aureus*. Additionally, this QCS@PVA/CA@PVA nanofabric was found to enhance wound healing.

While the QCS@PVA/CA@PVA nanofabric showcased efficient, hemostatic performance, biocompatibility, biodegradability, antimicrobial activity, and wound sealing ability, our study identified a limitation. The electrostatic interaction between the nanofibers proved to be pH-sensitive, rendering the nanofabric pH-dependent. This characteristic may restrict its applicability for wounds in acidic environments, such as the stomach. To address this issue, our future research aims to incorporate pH-independent noncovalent cross-linking or dynamic covalent cross-linking mechanisms into the nanofabric to bolster its stability under extreme pH conditions.

In conclusion, we have developed a blood-triggered self-sealing and tissue adhesive hemostatic nanofabric. The innovative hemostatic approach introduced in this research shows promising potential for significantly improving the effectiveness of wound dressings.

Methods

Materials

PVA (weight-average molecular weight (M_w) of 2×10^4, 98-99% hydrolyzed), 1-(3-dimethylaminopropyl)-3-ethylcarbodiimide hydrochloride (EDC), N-hydroxy-succinimide (NHS), dopamine hydrochloride (DA), 25% glutaraldehyde, and acetic acid were obtained from Aladin Biochemical Technology Co., Ltd. (Shanghai, China). Phosphate buffered saline (PBS, pH = 7.4) was from Biosharp Biochemical Technology Co., Ltd. 2-N-morpholino-ethanesulfonic acid buffer (MES buffer, pH = 5.5) was purchased from Shanghai Yuanye Biotechnology Co., Ltd. Sodium alginate (SA, M_w of 11×10^4 g/mol, guluronic-to-mannuronic ratio of 1.56) was gained from Sinopdrug Group Chemical Reagent Co., Ltd. Quaternized chitosan (QCS, 98% degree of quaternization), Fluorescein isothiocyanate (FITC) and Rhodamine B were purchased from Shanghai Macklin Biochemistry Co., Ltd. Fetal bovine serum (FBS) and trypsin-EDTA were gained from Bovogen Biologicals Pty Ltd. Isoflurane was provided by RWD Life science Co., Ltd. Fresh porcine skins and pig organs were acquired from a local market. The male Sprague Dawley (SD) rats with a weight of 200–250 g, female Landrace pigs with the weight of 30 kg, and guinea pigs with the weight of 300 g were provided from Slack Experimental Animal Co., Ltd. (Shanghai, China). The sex of animals has no influence on the results of the study.

Preparation of CA

2 g of SA was dissolved in 200 mL of MES buffer. Subsequently, 0.4 g each of EDC and NHS were dissolved in 40 mL of MES buffer. The resulting mixture was then slowly added dropwise to the SA solution, followed by the addition of 0.8 g of DA. The reaction took place over a period of 4 h at 5 °C under a nitrogen atmosphere. After the reaction, the solution underwent dialysis using an aqueous solution of HCl (pH = 5.5) for 48 h, followed by deionized water for an additional 24 h. Finally, the solution was freeze-dried to obtain catechol-modified SA,

https://doi.org/10.1038/s41467-025-60244-z

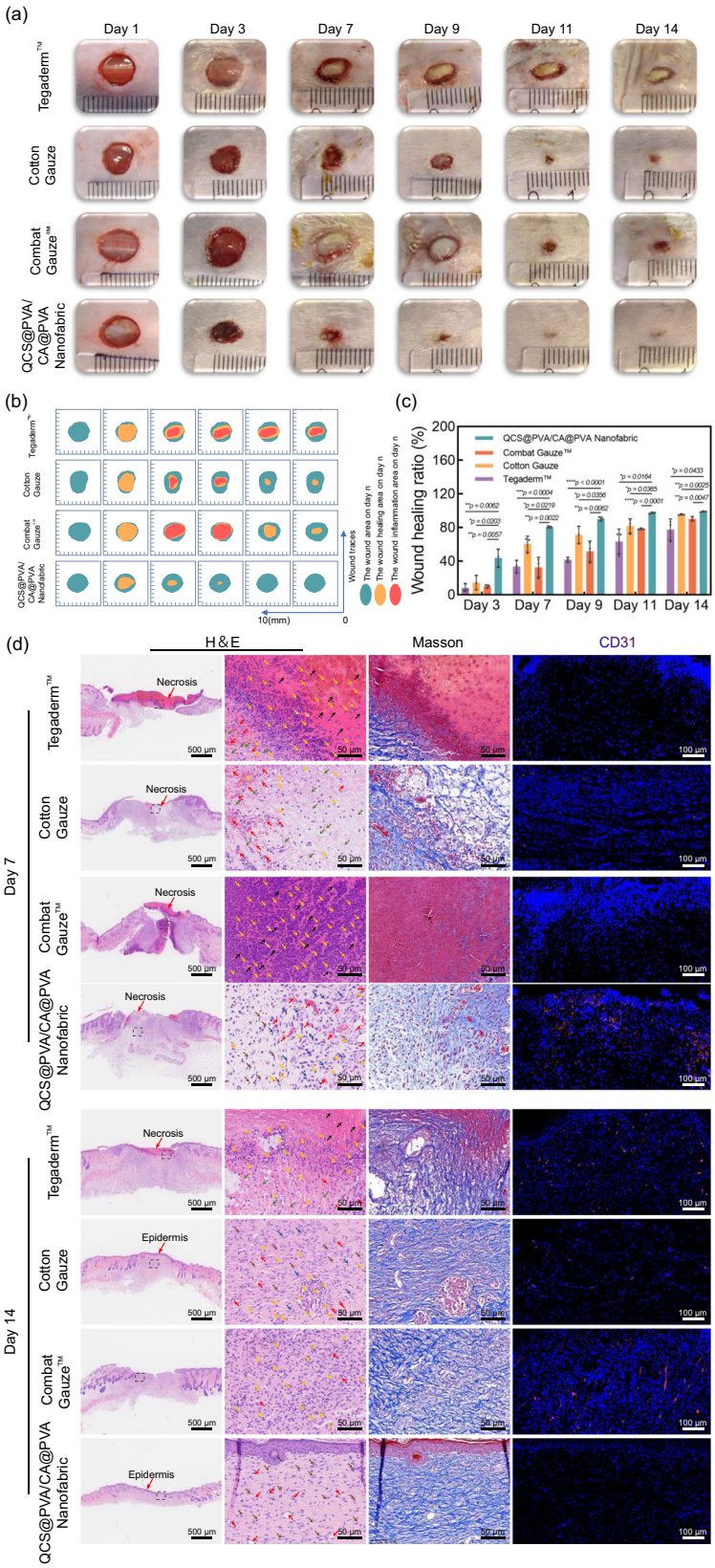

Fig. 8 | In vivo full-thickness skin wound healing of QCS@PVA/CA@PVA nanofabric. a Photographs of wound healing process by Tegaderm™, Combat Gauze™, cotton gauze, and QCS@PVA/CA@PVA nanofabric at the 1st day, 3rd day, 7th day, 9th day, 11th day and 14th day. **b** Wound traces and **c** wound healing ratios within 14 days of each group. $n = 3$ independent samples; Student's t test; two-tailed; error bars = SD; data are presented as mean ± SD; $^{*}p < 0.05$; $^{**}p < 0.01$; $^{***}p < 0.001$; $^{****}p < 0.000$). **d** H&E, Masson staining, and immunofluorescence images of CD31 staining (red) of wounds sections from each group at 7th day and 14th day. (Gray box: Local enlarged area; black arrow: plasma; yellow arrow: inflammatory cell; red arrow: blood capillary; green arrow: collagen fiber; blue arrow: fibroblast cell; brown arrow: fibrocyte; gray arrow: appendage) The representative images in a and d are shown from three independent mice.

referred to as CA. ^{1}H NMR and UV-vis spectroscopy were employed to verify the synthesis of CA. As depicted in Supplementary Fig. 14, new peaks between 6.5 ppm and 6.8 ppm corresponding to the catechol ring, and peaks between 2.8 ppm and 3.0 ppm attributed to the methylene of dopamine, were observed in the ^{1}H NMR spectrum of SADA[41]. Additionally, a peak around 280.0 nm appeared in the UV-vis profile of SADA (Supplementary Fig. 15). These results confirmed that dopamine was successfully conjugated onto the SA backbone. Based on UV-vis absorbance, the degree of catechol substitution onto SA was determined to be 17%, calculated according to the formula: (absorbance of CA - absorbance of SA) / absorbance of the calibration curve × 100% at 280 nm.

Preparation of FITC-labeled QCS and Rhodamine B-labeled CA

0.18 g QCS was dissolved in 20 mL of 0.1 mol/L acetic acid before adding 20 mL of methanol to the solution while stirring continuously. 10 mg of FITC was dissolved in 10 mL of methanol was gently added to the QCS solution. The reaction occurred in the dark at room temperature for 8 h. The mixture underwent dialysis using methanol for 24 h. Finally, the solution was freeze-dried to obtain FITC-labeled QCS. For the preparation of Rhodamine B-labeled CA, 0.01 g of Rhodamine B was dissolved in 10 ml of deionized water. Subsequently, 0.05 g of EDC and 0.04 g of NHS were added to the Rhodamine B solution. The mixture was stirred for 0.5 h before adding 30 mL of a 6 g/L CA solution. The resulting mixture was stirred in the dark at room temperature for 48 h. Unreacted Rhodamine B and other contaminants were removed through dialysis using ethanol. Finally, the product was obtained by freeze-drying the mixture to yield Rhodamine B-labeled CA.

Preparation of QCS@PVA/CA@PVA nanofabric, QCS@PVA nanofabric, CA@PVA nanofabric, and PVA nanofabric

QCS@PVA/CA@PVA nanofabric was produced using a dual coaxial electrospinning method. Initially, a 6 wt% PVA solution was prepared by dissolving PVA in deionized water. Following this, a 1.5 wt% QCS solution was created by dissolving QCS in deionized wate, while a 1 wt% CA solution was prepared by dissolving CA in deionized water. Each solution was loaded into a 5 mL syringe. Two syringes, respectively containing PVA and QCS, were attached to a coaxial needle setup, with PVA as the core and QCS as the shell. Similarly, two syringes, respectively containing PVA and CA were attached to another coaxial needle setup, with PVA as the core and CA as the shell. These two coaxial setups were placed on separate spray head holders. The electrospinning process was carried out using an electrospinning machine (PS-1+, Pansi Technology Co., Ltd., China) at 20 kV voltage and 25% relative humidity, with flow rates of 0.4 mL/h and a needle-to-receiver distance of 20 cm. For the production of QCS@PVA nanofabric, all operational conditions were identical to those for preparing QCS@PVA/CA@PVA nanofabric, except for substituting CA with QCS. Similarly, to fabricate CA@PVA nanofabric, CA was used instead of QCS, following the same procedures as for QCS@PVA/CA@PVA nanofabric. To produce PVA nanofabric, both QCS and CA were replaced by PVA, and the process mirrored that of preparing QCS@PVA/CA@PVA nanofabric.

Characterization

Fourier transform infrared spectra (FT-IR) were examined with a Fourier infrared spectrometer (Nicolet 5700, Thermo Scientific Nicolet, USA). Proton nuclear magnetic resonance (^{1}H NMR) spectra were measured using a nuclear magnetic resonance spectrometer (Bruker400 M; Switzerland, Germany). UV-visible (UV-vis) spectra were recorded with an ultraviolet spectrophotometer (PE LAMD850). The distribution of anionic nanofibers and cationic nanofiber fibers was observed an inverted Fluorescence Microscope (TS2R-FL, Nikon, Japan). The SEM images were collected using a scanning electron microscope (SEM, Regulus 8100, Hitachi, Japan) at a voltage of 10 kV. The TEM pictures and EDS mapping analysis were obtained using a transmission electron microscope (TEM, JEM-2100 Plus (JEOL, Japan). The absorbance (OD) level was acquired using a microplate reader (Multiskan FC, Thermo, USA).

Coagulation time

A hemostatic fabric measuring 20 × 20 mm^2 was placed in a 6-well plate, and 50 µL of citrate anticoagulant-treated SD rat blood was added. PBS was then introduced into the well at specific time intervals, and the clotting time of the material was recorded when no uncoagulated blood components were observed to be flushed out by PBS.

Blood Clotting Index

A hemostatic fabric measuring 20 × 20 mm^2 preheated at 37 °C for 20 min and then mixed with 50 µL of citrate anticoagulant-treated SD rat blood. The mixture was incubated at 37 °C for 5 min and subsequently washed with 10 mL of PBS solution. The blood clotting index (BCI) was determined using the formula:

$$\mathrm{BCI}\,(\%) = B_s/B_b \times 100\% \quad (1)$$

where B_s represents the absorbance of the supernatant in contact with the material's blood at 540 nm, and B_b is the absorbance of a mixture of 50 µL rat blood and 10 mL PBS at 540 nm.

Antibacterial Capability

Gram-positive *Staphylococcus aureus* (*S. aureus*, CMCC(B)26003) and Gram-negative *Escherichia coli* (*E. coli*, CMCC(B)44102) were utilized in the evaluation of the antibacterial properties of the materials. The bacterial strains were preserved in glycerol stocks at −80 °C. Prior to experiments, the strains were revitalized in Luria-Bertani (LB) liquid medium at 37 °C. The initial bacterial suspension concentration was quantified via the spread plate method, followed by serial dilution with sterile PBS to achieve a working concentration of 1×10^5 CFU/mL for subsequent experimental use. A 20 × 20 mm^2 hemostatic fabric was subjected to UV light exposure for 4 h. Following this, the materials were immersed in a 5 mL bacterial suspension (1×10^5 CFU/mL) at 37 °C for 12 h. Subsequently, 100 µL of the suspension was plated on solid agar and allowed to incubate at 37 °C for an additional 24 h. The antibacterial efficacy was determined using the formula:

$$\text{Antibacterial ratio}\,(\%) = (A - B)/A \times 100\% \quad (2)$$

where A and B represent the bacterial counts of the sample group and blank group without adding the sample, respectively.

Hemolysis Assay

The material was dispersed in PBS to create a suspension with concentrations of 0.5, 1, 2, and 4 mg/mL and then incubated for 10 min at 37 °C. Subsequently, 1 mL of each of the aforementioned samples was mixed with 1 mL of diluted blood ($V_{Blood}/V_{PBS} = 1/10$) and incubated at 37 °C for 1 h. The absorbance of the supernatant at 540 nm was utilized to calculate hemolysis using the formula:

$$\text{Hemolysis}\,(\%) = (AS - AP)/(AT - AP) \times 100\% \quad (3)$$

where A_S, A_P, and A_T represent the absorbance values of samples, PBS, and Triton X-100, respectively.

Cytotoxicity evaluation

Human umbilical vein endothelial cells (HUVECs, ATCC CRL-1730) were utilized as models to evaluate the cytocompatibility of hemostatic fabrics. Initially, the hemostatic fabrics underwent sterilization using pressure steam and were then placed in a 96-well plate. Subsequently, a cell suspension with a concentration of 1×10^4 cells/mL was

added for incubation at 37 °C in a 5% CO_2 incubator for 24 h. Following removal of the original media, 200 μL of fresh dulbecco's modified eagle medium with 10% fetal bovine serum and 20 μL of CCK-8 solution were added to each well. After 2 h of incubation, the absorbance at 450 nm was measured using a microplate reader, with the group containing media and cells as the control group. The group with only medium served as the blank. Cell viability was calculated using the formula:

$$\text{Cell viability}(\%) = Cs/Cc \times 100\% \quad (4)$$

where Cs and Cc represent the absorbances of the sample and control, respectively.

Animal experiments

All animal experiments were conducted in compliance with the regulations of the Research Animal Ethics Committee of Fujian Normal University (Animal Use Permit Number: SYXK (Min): 2020-0007). All animals were acclimatized for 7 days under controlled laboratory conditions, with ambient temperature maintained at 18–25 °C and relative humidity at 50–65%. The housing environment was kept quiet with scheduled ventilation and regular replacement of sterilized bedding to ensure hygiene.

In vivo degradation test and response evaluation

SD rats (18–22 g) were acclimatized and fed for 7 days, and then subcutaneous implantation was performed. The QCS@PVA/CA@PVA Nanofabrics were cut into squares with an area of 1*1 cm and sterilized with UV light for 1 h. After the mice were anesthetized, a transversal incision of about 1.5 cm was made at the middle side of their back to form a soft-tissue blind pouch. The UV-sterilized samples were placed into the blind bag, and the incision was sutured and the location of the embedded material was marked. Photographs were taken at regular intervals (day 1, day 7, day 14) to observe the degradation of the material in the mice and to euthanize the mice. The residual material was carefully removed from the tissues for weighing. The remaining tissues were fixed with 4% paraformaldehyde and stained with hematoxylin and eosin (H&E) then the stained slides were observed and analyzed by microscopy. IL-6, a pro-inflammatory cytokine, was employed to characterize the level of inflammatory response.

In vivo hemostatic evaluation in rat model

Various hemostatic fabrics, such as cotton gauze, Combat Gauze™, PVA nanofabric, QCS@PVA nanofabric, CA@PVA nanofabric, and QCS@PVA/CA@PVA nanofabric, were cut into 20×20 cm^2 squares, weighed, and their weights were recorded. Here, 18 SD rats were randomly divided into six groups (n = 3 rats per group), cotton gauze group, Combat Gauze™ group, PVA nanofabric group, QCS@PVA nanofabric group, CA@PVA nanofabric group and QCS@PVA/CA@PVA nanofabric group. To simulate rat liver noncompressible hemorrhage, a laparotomy was performed to expose the liver, followed by creating a 10 mm long and 5 mm high incision using a surgical blade to induce liver injury. Upon observing blood seepage, hemostatic materials were promptly applied to the wound. The amount of blood loss and bleeding time were then documented. In the case of rat femoral artery hemorrhage, the rat's femoral artery was severed using a surgical blade. Once blood started to seep out, the materials were immediately applied to the wound and pressure was maintained for 30 s. Subsequently, the pressure was released, and the bleeding was closely monitored. The amount of blood loss and bleeding time were recorded.

In vivo hemostatic evaluation in pig model

6 landrace pigs were randomly divided into two groups (n = 3 landrace pigs per group), Combat Gauze™ group and QCS@PVA/CA@PVA nanofabric group. Then, Landrace pigs were anesthetized with propofol. The femoral artery was transected using a sterile surgical blade. Two layers of QCS@PVA/CA@PVA measuring 50 × 50 mm^2 were placed over the wound, and pressure was manually applied for 30 s. Subsequently, the pressure was release,d and the bleeding was monitored. The amount of blood loss and bleeding time were documented. Combat Gauze™ was used as the control group.

In vivo wound healing

Rats were fed adaptively for one week prior to being anesthetized with isoflurane. Their backs were then shaved and disinfected with 70% alcohol to create an 8 mm diameter circular wound on each rat's back. The initiation of administration was marked as the 1st day after model establishment, with subsequent measurements taken on days 0, 3, 7, 9, 11, and 14. Tegaderm™ was used to cover the wounds of the blank control group, while experimental groups were treated with different materials. Throughout the observation period, wound diameter was measured using vernier calipers, and the wound healing rate was calculated using the formula:

$$\text{Wound healing ratio}(\%) = (S_1 - S_n)/S_n \times 100\% \quad (5)$$

where S_1 represents the wound area on the 1st day and S_n represents the wound area on a specific day. Additionally, on the 7th and 14th days, the healed skin was collected for hematoxylin and eosin (H&E) staining, Masson trichrome staining, and CD31 immunofluorescence staining.

Erythrocytes and platelets adhesion

Erythrocyte-rich plasma was prepared by centrifuging diluted rat anticoagulated blood (blood: PBS = 1:9 v/v) at 110 x g for 10 min at 4 °C. Subsequently, 200 μL of the erythrocyte-rich plasma was applied to each 20 × 20 mm^2 sample and incubated for 30 min at 37 °C. The samples underwent three washes with PBS to eliminate nonadherent erythrocytes. Following this, 5 mL of deionized water was added to lyse the adherent erythrocytes at 37 °C for 2 h. The absorbance value of the supernatant at 540 nm was then measured. A control group consisting of 100 μL of erythrocyte suspension in 5 mL of deionized water was used for comparison. The erythrocyte adhesion ratio was calculated using the formula:

$$\text{Erythrocyte adhesion}(\%) = E_s/E_r \times 100\% \quad (6)$$

where E_s and E_r represent the absorbance values of the sample and control group, respectively.

Platelet-rich plasma was obtained from rat anticoagulated blood by centrifugation at 110 x g for 10 min at 4 °C. Each 20 × 20 mm^2 sample was treated with 100 μL of platelet-rich plasma and then incubated at 37 °C for 30 min. Subsequently, nonadherent platelets were washed with PBS. The samples were then immersed in 1 mL of 1% Triton X-100 at 37 °C for 1 h to fully lyse the adhering platelets. The level of released lactate dehydrogenase was assessed using an LDH kit from Beyotime Biotechnology, Shanghai, China, and the absorbance of the supernatant at 490 nm was measured. A control group, consisting of 100 μL of Platelet-rich plasma in 1 mL of 1% Triton X-100, was used for comparison. The platelets' adhesion ratio was calculated using the formula:

$$\text{Platelets adhesion}(\%) = P_s/P_r \times 100\% \quad (7)$$

Here, P_s represents the absorbance of the sample and P_r represents the absorbance of the control group.

To investigate the adhesion behavior of erythrocytes and platelets on hemostatic fabrics, 100 μL of erythrocyte-rich plasma or platelet-rich plasma was added to each sample and incubated at 37 °C for 1 h. Subsequently, the samples were washed three times with PBS to eliminate any nonadherent erythrocytes or platelets. Following this, the samples were fixed with 2.5% glutaraldehyde, dehydrated gradually using ethanol concentrations ranging from 10% to 100% for 10 min each, and finally observed using SEM.

In vivo sensitization experiment

18 healthy guinea pigs (weight 300 g, skin disease-free) were randomly divided into 3 groups (6 per group): negative control group (normal saline), positive control group (10% sodium dodecyl sulfate), and QCS@PVA/CA@PVA nanofabric group. Prior to the experiment, nanofiber materials were sterilized by ultraviolet irradiation for 1 h, and material extracts were prepared using the physiological saline extraction method. Each group received topical application of 0.2 mL corresponding test substance on depilated skin areas. Skin allergic reactions were observed and recorded 6 h post-administration. Seven days after the first sensitization, a second sensitization was performed using identical procedures, with immediate observation of skin reactions and systemic status. Seven days after the second sensitization, the substances were re-administered. Skin allergic reactions were observed 6 h post-administration, while skin edema, erythema severity at challenge sites, and systemic conditions were systematically evaluated at 24 and 48 h post-administration.

The skin irritation response is classified into four grades (0–4) based on the clinical manifestations of erythema and edema: erythema ranges from no erythema, mild erythema with indistinct borders, moderate bright red erythema with clear borders, severe dark red erythema accompanied by congestion, to extreme severe purplish-red erythema with eschar formation; edema progresses from no edema, mild edema with slight edge elevation, 1 mm clearly defined elevation, localized significant elevation >1 mm, to extensive edema involving surrounding tissues. The total irritation score is calculated using the formula:

$$\text{Total Irritation Score} = (E_r + E_d)/T \quad (8)$$

where, E_r represents the sum of erythema scores, E_d represents the sum of edema scores and T represents the total number of test animals. Based on this score, irritation intensity is categorized as follows: 0–0.49 indicates no irritation, 0.50–2.99 mild irritation, 3.00–5.99 moderate irritation, and 6.00–8.00 severe irritation.

Water vapor transmission rate

A sample measuring 20 × 20 mm^2 was placed over a beaker containing 10 mL of distilled water to assess water vapor permeability. The decrease in water mass in the beaker after 24 h at 37 °C was recorded. The water vapor transfer rate was calculated according to the formula:

$$\text{water vapor transfer rate} = (M_i - M_f)/A \quad (9)$$

where A represents the area of the beaker mouth in square meters, and M_i and M_f denote the initial and final weights of the beaker post water evaporation, respectively.

Lap shear test

The adhesion strength was assessed through lap shear testing conducted on a LR5K universal testing machine equipped with a 100 N load cell. A piece of wet porcine tissue measuring 50 × 15 mm^2 was first wetted with 20 μL of blood and then covered by a 15 × 15 mm^2 sample. Subsequently, another piece of wet porcine tissue of the same size was pressed onto the sample side and left in place for 30 s. The shear strength was determined using the formula:

$$\text{Shear strength} = F/A \quad (10)$$

where A (m^2) represented the material's contact area with the tissue, and F (N) was the force at the point of fracture.

Resistance to permeation by water

A glass tube measuring 200 mm in height and 23 mm in diameter was secured on an iron frame. Two layers of QCS@PVA/CA@PVA nanofabric (50 × 50 mm^2) were directly wrapped around one end of the glass tube. Subsequently, Rhodamine B dyed distilled water was introduced into the opposite end of the glass tube. The water penetration of the membrane was documented using digital photographs. Due to poor adhesion of cotton gauze, Combat Gauze™, PVA nanofabric, QCS@PVA nanofabric, and CA@PVA nanofabric, they required tape to be held in place at the opening of the glass tube.

Bursting pressure test

The apparatus was built using a tee pipe, connected on one end to an argon pressure gauge for monitoring pressure, and on the other end to a glass tube with a 6 mm inner diameter via a silicone tube. The surface of the glass tube was wetted with water and sealed with a material measuring 30 × 30 mm^2. A silicone catheter was utilized to connect the third end to a peristaltic pump, mimicking the natural flow of human blood. The maximum value on the pressure gauge indicated the material's resistance to burst pressure.

Demonstration for real-life applications

The experiments were performed with the assistance of volunteers, and informed consent was obtained for the publication of images.

Statistical analysis

All tests were repeated independently and conducted at least three times. The Student's *t*-test was used for statistical analysis in GraphPad Prism 9.4 and Origin 2018. (ns = not significant; $^{*}p < 0.05$; $^{**}p < 0.01$; $^{***}p < 0.001$; $^{****}p < 0.000$). The results of histology, wound healing ratio, and fluorescence intensity are quantitatively analyzed using Image-Pro Plus 6.0 and SlideViewer 2.5.0.

Reporting summary

Further information on research design is available in the Nature Portfolio Reporting Summary linked to this article.

Data availability

Source data are provided with this paper. All experimental data within the article and its Supplementary Information are available from the corresponding authors upon request. The source data of Figs. 1i, 3c, g, h, 4b, d, f, h, j, k, 5b, c, e, f, 6c, d, f, g, 6j, k, 8c and Supplementary Figs. 1, 7a, b, c, 11b, c, 13a, b, 14, 15 are provided as a Source Data file. Source data are provided with this paper.

References

1. Montazerian, H. et al. Engineered hemostatic biomaterials for sealing wounds. *Chem. Rev.* **122**, 12864–12903 (2022).
2. Hsu, B. B. et al. Clotting mimicry from robust hemostatic bandages based on self-assembling peptides. *ACS Nano* **9**, 9394–9406 (2015).
3. Zhong, Y. et al. Application and outlook of topical hemostatic materials: a narrative review. *Ann. Transl. Med.* **9**, 577–577 (2021).
4. Bu, Y. et al. Tetra-PEG based hydrogel sealants for in vivo visceral hemostasis. *Adv. Mater.* **31**, 1901580 (2019).
5. He, H. et al. Efficient biosafe and tissue adhesive hemostatic cotton gauze with controlled balance of hydrophilicity and hydrophobicity. *Nat. Commun.* **13**, 552 (2022).

6. Fang, Y. et al. 3D porous chitin sponge with high absorbency, rapid shape recovery, and excellent antibacterial activities for non-compressible wound. *Chem. Eng. J.* **388**, 124169 (2020).
7. Leonhardt, E. E., Kang, N., Hamad, M. A., Wooley, K. L. & Elsabahy, M. Absorbable hemostatic hydrogels comprising composites of sacrificial templates and honeycomb-like nanofibrous mats of chitosan. *Nat. Commun.* **10**, 2307 (2019).
8. Peng, X. et al. Ultrafast self-gelling powder mediates robust wet adhesion to promote healing of gastrointestinal perforations. *Sci. Adv.* **7**, eabe8739 (2021).
9. Du, X. et al. Microchannelled alkylated chitosan sponge to treat noncompressible hemorrhages and facilitate wound healing. *Nat. Commun.* **12**, 4733 (2021).
10. Yuk, H. et al. Rapid and coagulation-independent haemostatic sealing by a paste inspired by barnacle glue. *Nat. Biomed. Eng.* **5**, 1131–1142 (2021).
11. Lu, X., Li, X., Yu, J. & Ding, B. Nanofibrous hemostatic materials: structural design, fabrication methods, and hemostatic mechanisms. *Acta Biomater.* **154**, 49–62 (2022).
12. Cui, Y. et al. Robust hemostatic bandages based on nanoclay electrospun membranes. *Nat. Commun.* **12**, 5922 (2021).
13. Chen, X. et al. Hydrogel bioadhesives with extreme acid-tolerance for gastric perforation repairing. *Adv. Funct. Mater.* **32**, 2202285 (2022).
14. Liu, C. et al. Trojan-horse mineralization of trigger factor to impregnate non-woven alginate fabrics for enhanced hemostatic efficacy. *Carbohydr. Polym.* **320**, 121213 (2023).
15. Tan, Y., Yang, Q., Zheng, M., Sarwar, M. T. & Yang, H. Multifunctional nanoclay-based hemostatic materials for wound healing: a review. *Adv. Healthc. Mater.* **13**, 2302700 (2024).
16. Zhu, T. et al. Superhydrophobic/superhydrophilic Janus fabrics reducing blood loss. *Adv. Healthc. Mater.* **7**, 1701086 (2018).
17. Li, Z. et al. Superhydrophobic hemostatic nanofiber composites for fast clotting and minimal adhesion. *Nat. Commun.* **10**, 5562 (2019).
18. Dong, Y. et al. Safe and efficacious near superhydrophobic hemostat for reduced blood loss and easy detachment in traumatic wounds. *ACS Appl. Mater. Interfaces* **16**, 4307–4320 (2024).
19. Tang, H. et al. Injectable ultrasonic sensor for wireless monitoring of intracranial signals. *Nature* **630**, 84–90 (2024).
20. Fang, Y. et al. Gluing blood into adhesive gel by oppositely charged polysaccharide dry powder inspired by fibrin fibers coagulation mediator. *Carbohydr. Polym.* **333**, 121998 (2024).
21. Li, C. et al. Rational design of Lewis base molecules for stable and efficient inverted perovskite solar cells. *Science* **379**, 690–694 (2023).
22. Park, Y. S. & Kang, S. W. Role of ionic liquids in enhancing the performance of the polymer/$AgCF_3SO_3$/$Al(NO_3)_3$ complex for separation of propylene/propane mixture. *Chem. Eng. J.* **306**, 973–977 (2016).
23. Deng, J. et al. Plant-based shape memory cryogel for hemorrhage control. *Adv. Mater.* **36**, 2311684 (2024).
24. Geng, Z. et al. Preparation and characterization of a dual cross-linking injectable hydrogel based on sodium alginate and chitosan quaternary ammonium salt. *Carbohydr. Res.* **507**, 108389 (2021).
25. Zhu, X. et al. A cation-methylene-phenyl sequence encodes programmable poly(ionic liquid) coacervation and robust underwater adhesion. *Adv. Funct. Mater.* **32**, 2105464 (2021).
26. Okada, A., Miura, T. & Takeuchi, H. Protonation of histidine and histidine-tryptophan interaction in the activation of the M2 ion channel from influenza a virus. *Biochemistry* **40**, 6053–6060 (2001).
27. Ma, Z., Bao, G. & Li, J. Multifaceted design and emerging applications of tissue adhesives. *Adv. Mater.* **33**, 2007663 (2021).
28. Singh, G. & Chanda, A. Mechanical properties of whole-body soft human tissues: a review. *Biomed. Mater.* **16**, 062004 (2021).
29. Zhang, K. et al. Gelable and adhesive powder for lethal non-compressible hemorrhage control. *Adv. Funct. Mater.* **33**, 2305222 (2023).
30. Mao, X., Yuk, H. & Zhao, X. Hydration and swelling of dry polymers for wet adhesion. *J. Mech. Phys. Solids* **137**, 103863 (2020).
31. Li, J. et al. Tough adhesives for diverse wet surfaces. *Science* **357**, 378–381 (2017).
32. Maier, G. P., Rapp, M. V., Waite, J. H., Israelachvili, J. N. & Butler, A. Adaptive synergy between catechol and lysine promotes wet adhesion by surface salt displacement. *Science* **349**, 628–632 (2015).
33. Westerman, C. R., McGill, B. C. & Wilker, J. J. Sustainably sourced components to generate high-strength adhesives. *Nature* **621**, 306–311 (2023).
34. Chen, Y. et al. Tough and on-demand detachable wet tissue adhesive hydrogel made from catechol derivatives with a long aliphatic side chain. *Adv. Healthc. Mater.* **12**, 2301913 (2023).
35. Kean, T. & Thanou, M. Biodegradation, biodistribution and toxicity of chitosan. *Adv. Drug Deliv. Rev.* **62**, 3–11 (2010).
36. Li, M., Shang, Q., Li, G., Wang, X. & Yu, G. Degradation of marine algae-derived carbohydrates by bacteroidetes isolated from human gut microbiota. *Mar. Drugs* **15**, 92 (2017).
37. Li, M. et al. In vitro fermentation of alginate and its derivatives by human gut microbiota. *Anaerobe* **39**, 19–25 (2016).
38. Zhong, Y. et al. Construction methods and biomedical applications of PVA-based hydrogels. *Front. Chem.* **12**, 1376799 (2024).
39. Xu, H. et al. Green fabrication of amphiphilic quaternized β-chitin derivatives with excellent biocompatibility and antibacterial activities for wound healing. *Adv. Mater.* **30**, 1801100 (2018).
40. Liu, Z. et al. Hyperbranched catechol biomineralization for preparing super antibacterial and fire-resistant soybean protein adhesives with long-term adhesion. *Chem. Eng. J.* **449**, 137822 (2022).
41. Huang, W. et al. Noncompressible hemostasis and bone regeneration induced by an absorbable bioadhesive self-healing hydrogel. *Adv. Funct. Mater.* **31**, 2009189 (2021).
42. Zhang, K. et al. Tough hydrogel bioadhesives for sutureless wound sealing, hemostasis and biointerfaces. *Adv. Funct. Mater.* **32**, 2111465 (2022).
43. Wang, H. et al. A super tough, rapidly biodegradable, ultrafast hemostatic bioglue. *Adv. Mater.* **35**, 2208622 (2023).
44. Hong, Y. et al. A strongly adhesive hemostatic hydrogel for the repair of arterial and heart bleeds. *Nat. Commun.* **10**, 2060 (2019).
45. Wu, J. et al. An off-the-shelf bioadhesive patch for sutureless repair of gastrointestinal defects. *Sci. Transl. Med.* **14**, abh2857 (2022).
46. Wang, H. et al. An integrally formed Janus hydrogel for robust wet-tissue adhesive and anti-postoperative adhesion. *Adv. Mater.* **35**, 2300394 (2023).

Acknowledgements

This work was supported by the National Natural Science Foundation of China under Grant No. 52103108 (Yan Fang) and No. 22175037 (Haiqing Liu).

Author contributions

Yan Fang conceived the idea and wrote the manuscript. Linyu Wang completed all the experiments. Xinwei Zheng, Peng Ni, Zhibo Xu, and Ziying Wang assisted with animal experiments. Yunxiang Weng, Qinhui Chen, and Haiqing Liu supervised the research.

Competing interests

The authors declare no competing interests.

Additional information

Supplementary information The online version contains supplementary material available at https://doi.org/10.1038/s41467-025-60244-z.

Correspondence and requests for materials should be addressed to Qinhui Chen or Haiqing Liu.

Peer review information *Nature Communications* thanks the anonymous reviewers for their contribution to the peer review of this work. A peer review file is available.